

The Hypno-PC: Uncovering Sleep Dynamics through Principal Component Analysis and Hidden Markov Modeling of Electrophysiological Signals

Author information:

Dr. Miriam Guendelman (corresponding author)

Department of Cognitive and Brain Sciences, Ben-Gurion University of the Negev, Beer-Sheva, Israel, 8410501.

Email: miriamg@post.bgu.ac.il, miriam.guen@gmail.com

ORCID ID: 0000-0003-3708-7763

Phone: +9725026216202

Prof. Oren Shriki

Department of Cognitive and Brain Sciences, Ben-Gurion University of the Negev, Beer-Sheva, Israel, 8410501.

Email: shrikio@bgu.ac.il

ORCID ID: 0000-0003-1129-4799

Phone: +972542628555

Abstract

Manual sleep scoring segments sleep into discrete 30-s epochs (wake, NREM 1–3, REM), yet substantial evidence suggests that sleep unfolds as a continuous, microstate-rich process. Using a data-driven approach, we analysed overnight high-density EEG, EOG, EMG, and ECG recordings from 29 healthy adults (ANPHY-Sleep dataset). Signal-specific features from standard 30-s and finer 4-s epochs were compressed using principal component analysis (PCA). With the 30-s epochs, the first principal component (Hypno-PC; 42% variance) closely tracked the hypnogram, while the extended PCA space (explaining 90% variance) achieved sleep-stage separability comparable to the state-of-the-art YASA classifier. Furthermore, Hypno-PC emphasised continuous sleep dynamics, revealing a gradual descent into deep NREM sleep contrasted with abrupt transitions into REM or wakefulness.

Independent component analysis (ICA) on the top principal components ($n=5$) separated spindle-rich, slow-wave-dominant, and arousal-related processes. A Gaussian hidden Markov model (GHMM) fitted to ICA features identified four macrostates at 30-s resolution, aligning closely with canonical sleep stages ($\text{Kappa} = 0.70$). These macrostates required minimal labelling (<1% of epochs) and provided highly accurate estimates of sleep-onset latency. At a finer 4-s resolution, the GHMM resolved eleven microstates, distinguishing tonic from phasic REM, active from quiet wakefulness, and early- from late-night NREM subtypes. Three hub states—active wake, N1-like, and late slow-wave-rich—mediated most microstate transitions, highlighting structured continuity within sleep microstate architecture.

This linear, interpretable PCA–ICA–GHMM framework bridges conventional sleep staging, continuous sleep dynamics, and detailed microstate structure, offering clinicians and researchers a scalable, objective tool for studying sleep architecture.

Keywords

High-density EEG; Continuous sleep processes; Sleep microstates; Automated polysomnography analysis; Unsupervised machine learning in sleep; Principal Component Analysis (PCA); Independent Component Analysis (ICA); Gaussian Hidden Markov Model (GHMM).

Statement of Significance

This study introduces a data-driven framework that bridges traditional sleep scoring and the intrinsic continuity of human sleep. Using high-density EEG, EOG, EMG, and ECG, we derive a low-dimensional space that captures sleep architecture through unsupervised methods. The leading dimension, explaining most of the signal's variability, faithfully tracks the hypnogram while revealing gradual descents into deep NREM and abrupt shifts into REM or brief awakenings. We further reveal spindle-rich, slow-wave, and arousal components and identify data-driven states closely aligning with canonical sleep stages. At finer temporal resolution, we uncover structured microstates, distinguishing tonic versus phasic REM and early versus late NREM. Our interpretable PCA–ICA–GHMM pipeline thus provides clinicians and researchers with a scalable tool for objective sleep phenotyping.

Introduction

Accurately characterising how brain activity changes during sleep is central in neuroscience and clinical sleep medicine. The current clinical gold standard—polysomnography (PSG) scored according to American Academy of Sleep Medicine (AASM) rules—assigns each 30-second epoch to wake, rapid-eye-movement (REM) sleep, or one of three non-REM stages (N1–N3) by visually inspecting electroencephalography (EEG), electrooculography (EOG), electromyography (EMG), and electrocardiography (ECG) traces [1]. Characteristic rhythms guide this labelling: posterior alpha marks quiet wakefulness; frontal theta dominates N1 and REM; sigma spindles define N2; and high-amplitude delta slow waves indicate N3, with autonomic indices such as heart-rate variability complementing stage boundaries [2, 3].

Manual stage classification compresses sleep architecture into the five stages, historically defined for low-density PSG montages and 30-s epochs. While this simplification helps clinicians interpret large datasets and understand core sleep processes, it also discards valuable spatial, spectral, and temporal information—particularly in high-density recordings, potentially obscuring physiologically meaningful patterns [4–6]. Thus, the critical question is not whether to create such a simplification but rather how best to do so. Specifically, can we use data-driven methods to uncover the latent structure of sleep directly from the physiological signals—preserving regional detail and temporal continuity—instead of forcing it into the traditional five-stage model?

Low-dimensional embeddings of sleep dynamics

Dimensionality reduction methods have proven valuable in neuroscience, enabling researchers to capture and interpret complex neuronal population dynamics concisely and meaningfully [7].

In sleep research, advanced data-driven approaches—including t-distributed stochastic neighbour embedding (t-SNE), uniform manifold approximation (UMAP), diffusion maps, and deep auto-encoders—have successfully projected whole-night EEG and fMRI recordings into low-dimensional manifolds. These methods effectively separate wake, REM, and NREM sleep, revealing even finer micro-patterns [8,9]. Despite their power to capture intricate geometries and nonlinear interactions, these advanced nonlinear transformations often make it challenging to directly interpret specific underlying frequencies, electrode channels, or autonomic features, thus limiting their interpretability and, consequently, their clinical utility.

Linear dimensionality reduction provides an interpretable bridge between complex polysomnographic signals and clinically meaningful constructs. Principal-component analysis (PCA) first rotates the multivariate feature space to the directions that maximise variance, producing orthogonal axes ranked by the amount of variability each captures [10]. A recent study showed that a single PCA component derived from spectral features of three EEG leads could track continuous sleep depth and trace the hypnogram without requiring labeled data [11].

However, PCA's orthogonality constraint can blur distinct physiological processes that co-vary during sleep. Independent-component analysis (ICA) can address this limitation; this approach can be used to find statistically independent process-specific axes within the PCA subspace [12]. Applying ICA after an initial PCA clean-up improves numerical stability and focuses the decomposition on the most informative variance.

Because both steps are linear, every component is an explicit weighted sum of the original physiological features; investigators can identify the frequencies, channels, or autonomic measures that drive a latent axis. This way, the driving features of each PCA or ICA dimension remain visible, facilitating direct comparison with existing physiological and clinical knowledge.

Capturing temporal structure

Static embeddings ignore the ordered grammar of sleep. In order to model the temporal dimension, we modelled the embedded sequence with a Gaussian hidden Markov model (GHMM) [13]. The GHMM fuses information from two sources—(i) the low dimensional representation of the current state (emission probabilities) and (ii) the likelihood of a transition from the previous state (transition probabilities)—to infer latent states, quantify their stability, and chart the preferred pathways through the night, all while preserving the interpretability of the underlying linear features. In doing so, it operationalises the view of sleep as a biased stochastic drift across a continuum bounded by soft thresholds rather than rigid walls [14,15].

Study goals

We aimed to develop a transparent, fully automated pipeline that converts the richness of high-density PSG data into an interpretable map of sleep dynamics, enabling clinicians and researchers to trace findings back to specific brain oscillations and peripheral measures. Our objectives were fourfold: first, to compress multielectrode EEG, EOG, EMG, and ECG features—sampled at both the standard 30-s epoch and a finer 4-s window—into a linear low-dimensional space using PCA; second, to refine this PCA space using ICA, isolating independent physiological processes; third, to employ a GHMM to incorporate temporal context into the identification of latent sleep states; and fourth, with minimal supervision, to relate these latent states to canonical sleep stages, and leverage the linear interpretability to integrate our findings with established literature.

Thus, we tested whether our PCA–ICA–GHMM pipeline could reveal continuous sleep processes, coarse macrostates, and finer microstates, quantify their transition dynamics, bridge conventional sleep staging with these data-driven representations, and ultimately offer scalable tools to advance sleep research.

Methods

Data

We used the ANPHY-Sleep dataset [16], a publicly available resource containing PSG recordings of 29 healthy, normal sleepers. Each recording includes high-density EEG with 83 channels, two bipolar EOG channels, three bipolar EMG channels (legs and chin), and one bipolar ECG channel. The data were scored according to AASM guidelines [1], providing a reference hypnogram for each subject. Subject demographics are documented by Wei et al. 2024 [16].

Pre-processing

Current pre-processing aims to clean the raw signals and remove non-physiological noise sources. This step provides stable inputs for subsequent feature extraction and reduces the effect of systematic artefacts on the analysis. The pre-processing was performed using custom code and MNE-Python [17] functions. All signals were initially band-pass filtered, with the frequency bands adjusted to capture relevant information for each modality. The filters applied included EEG: 0.5–40 Hz, EOG: 0.3–15 Hz, EMG: 10–50 Hz, and ECG: 0.5–20 Hz.

We applied an average reference to the EEG channels. For EOG, we added a derived channel by referencing left EOG to right EOG to emphasise horizontal eye movements. Bipolar referencing was used for EMG and ECG. Signals were segmented into contiguous, non-overlapping epochs of 30 seconds and 4 seconds. These epochs form the fundamental time windows for feature extraction.

Feature Extraction

Feature extraction converts the raw signals into numerical summaries that reflect the physiological characteristics of the signal. This step distils large volumes of data into meaningful metrics that represent brain rhythms, muscle activity, eye movements, and cardiac dynamics. For each epoch, we computed the following:

EEG Features: We used the Welch method to estimate the power spectral density (PSD) at 0.5–40 Hz. Relative spectral power was extracted for low delta (0.5–1.5 Hz), high delta (1–4 Hz), theta (4–8 Hz), alpha (8–12 Hz), low sigma/high alpha (10–13 Hz), high sigma (12–16 Hz), beta (15–25 Hz), and gamma (25–40 Hz) bands. The aperiodic slope and intercept (from linear fits on log-log PSD), spectral entropy, and total power were also calculated using log-transformed spectral power.

EMG Features: PSD between 10 and 50 Hz was computed similarly, and total power in this range represented muscle activity.

EOG Features: Total spectral power between 0.3 and 2 Hz served as an index of eye movements.

ECG Features: After band-pass filtering the ECG (0.5–20 Hz), to boost the sharp QRS complexes and suppress slow baseline drift, we first took the first difference of the signal and squared it into a standard peak-enhancement step that magnifies steep, high-energy deflections before peak detection [18]. R-peaks were detected using the SciPy “find_peaks” function [19]. The resulting peak train yielded beat-to-beat (R–R) intervals, from which we computed heart rate (HR = 60 / mean RR), the standard deviation of normal-to-normal intervals (SDNN), and the root-mean-square of successive differences (RMSSD) [18]. HR-variability metrics are inherently noisy in 30 and 4-s windows. However, instead of treating this instability as an artefact, we used the relative fluctuations of SDNN and RMSSD over time as informative features, building on evidence that moment-to-moment autonomic changes track sleep depth and arousals [20]. Therefore, this time-resolved approach potentially retains short-scale autonomic dynamics rather than averaging them out.

Feature Cleaning and Standardisation

This step ensures that all extracted features are on a comparable scale and that missing or extreme values do not bias downstream analyses. It stabilises the dataset in order to apply PCA.

Within each subject, features were z-scored by subtracting the mean and dividing by the standard deviation. Missing values occurred only for the ECG measure at the 4-second resolution and in less than < 0.2% of the data in 12 subjects. Most missing values were found in subject EPCTL29, where RMSSD could not be calculated for 430 segments, likely due to a low HR, as at least three detected peaks are required for this calculation. To maintain temporal sampling consistency, missing values were linearly interpolated. To reduce the impact of outliers on the PCA features, values were clipped to the range of [-5, 5]. Across features, the mean portion of clipped values was lower than 1% of the segments, and no trend was observed in individual features.

Principal Component Analysis (PCA)

PCA reduces the complexity of the dataset by identifying orthogonal directions (principal components) of maximal variance. This step condenses a large number of features into a handful of variables, making the predominant patterns in the data easier to visualise and analyse.

PCA was applied to the standardised feature matrix pooled across all subjects, resulting in a common component space into which all individual data were projected. This shared space enables consistent interpretation of component dynamics and cross-subject comparisons. Recognising practical constraints in clinical settings, we conducted supplementary analyses using a reduced subset of six standard PSG electrodes: F3, F4, C3, C4, O1, and O2. PCA was recomputed based on this reduced montage for a complementary analysis.

Components explaining at least 2% of the total variance were retained, resulting in five principal components (PCs) in the complete montage layout and six PCs for the six-electrode version. These PCs were plotted over time and compared to the hypnogram to interpret their relation to known sleep stages.

Visualising Component Filters

We visualised how each physiological feature contributed to these abstract dimensions to enhance the interpretability of principal and independent components. We generated spatial topographies for EEG features by projecting component weights onto a head map based on the electrode layout. Non-EEG features, including EOG, EMG, and ECG signals, were visualised using bar plots. The colour in these maps highlights the feature loadings' direction and magnitude, facilitating a clear physiological interpretation of the components.

Statistical Analysis

We quantified the relationship between each principal or independent component and manually defined sleep stages to determine how reliably these components differentiated the sleep stages. For each component, we fitted a linear mixed-effects model using the Python package Statsmodels²¹ with the formula:

$$\text{Component} \sim 0 + \text{Stage} + (0 + \text{Stage} | \text{Subject})$$

This approach estimated the direction and magnitude of associations between components and sleep stages, explicitly modelling individual variability through random subject-specific slopes. We extracted regression coefficients, standard errors, p-values, and 95% confidence intervals from each model. Results were visualised to highlight significant differences between stages using conventional markers, and we plotted individual-subject slopes to assess the consistency of these relationships across subjects.

Supervised Separability Analysis Using Linear SVM

To quantify how well the PCA-derived low-dimensional feature space supports the differentiation of conventional sleep stages (wake, REM, N1, N2, N3), we conducted a supervised classification analysis using a linear support vector machine (SVM). Although our main framework is unsupervised, this supervised analysis served as a benchmark to evaluate the separability of manually scored stages within the PCA-derived representation.

Methodological Approach:

A linear SVM classifier (LinearSVC from scikit-learn) was trained and evaluated using leave-one-subject-out cross-validation (LOOCV). For each round, data from 28 subjects formed the training set for each iteration, while data from the left-out subject served as the independent test set (see the number of epochs per subject used in Supplementary Table 3). The PCA features were standardised before training, and balanced class weights were applied to mitigate potential class imbalances.

We assessed the classifier with successively larger PCA inputs—adding components one by one up to all 63 from the complete montage (or 22 from the six-electrode set), accounting for 90 % of the total variance. Classification evaluations were performed at the 30-second epoch resolution, where gold standard levels are defined.

Performance Evaluation Metrics

Classifier performance was comprehensively assessed using overall accuracy, Cohen's Kappa (Kappa), stage-specific precision, recall (sensitivity), and F1-score. Metrics were computed for each subject individually and averaged across subjects. We also computed 95% confidence intervals to quantify between-subject variability.

Benchmarking with Established Sleep Classifier (YASA)

We compared the linear SVM classifier performance against predictions from the widely validated YASA algorithm to benchmark our results within current automated sleep-scoring standards [22]. YASA employs a supervised algorithm utilising recommended EEG (C4-M1), EOG (LOC-M2), and EMG (chin) derivations, along with demographic data (age and gender). This benchmarking helped us assess how the supervised PCA-SVM staging compares against a validated clinical staging tool.

Independent Component Analysis (ICA)

ICA was applied to further decompose the principal components (PCs) into statistically independent processes, helping to isolate distinct physiological generators that might be mixed within the PCs. Applying ICA to this complete component set is computationally intensive and prone to convergence issues. PCA orthogonalised the feature space and retained the principal axes of variance ordered by the variance ratio they captured. Here, components explaining $\geq 2\%$ of the total variance were retained, removing low variance dimensions that can destabilise ICA. This pre-processing step ensures that ICA operates within a compact, well-conditioned subspace, facilitating the reliable extraction of independent physiological sources.

To further ensure robust separation, each PC was re-scaled before ICA training, and the model was fitted on the PCs using the Python-Picard package, which implements an extended infomax algorithm to separate both sub- and super-Gaussian signals [23]. After fitting, the ICA unmixing transformation was applied without unit scaling to preserve the original variance ratios of the identified processes. We then analysed the resulting independent component (IC) time series similarly to the PCs.

Gaussian Hidden Markov Model (GHMM)

While supervised sleep staging and approaches rely on pre-defined, pre-labelled sleep stages for training and evaluating the models, the GHMM approach [13] does not rely on such labels for either training or evaluation, providing potential temporal flexibility beyond the standard 30 seconds. The GHMM models data as observations generated by a sequence of hidden states, each characterised by a distinct distribution in the feature space and the probability of transitioning from a preceding state. As a result, this approach infers latent states and transition dynamics directly from the observed data structure without prior assumptions on pre-defined states. Thus, it captures the temporal structure of sleep, such as stage stability (via self-transitions) and sleep-state transitions [24].

In this work, we modelled each state's emissions as multivariate Gaussian distributions in the PCA or ICA-transformed spaces at both 30-second and 4-second resolutions and estimated model parameters using the expectation-maximisation (EM) [25] algorithm implemented in the “hmmlearn” Python library. This implementation was chosen for its simplicity and modularity. While the Gaussian assumption may not strictly hold for the representation of each state in these spaces, it provides a parsimonious model appropriate for our modest sample size ($N = 29$). Given the potential for overfitting in more flexible models (e.g., Gaussian mixtures or semi-Markov formulations), we opted for a single Gaussian (rather than a mixture) structure to balance expressiveness and robustness.

A key hyperparameter in this model is the **number of states** it is designed to model. In contrast to supervised modelling, where we know the exact number of states, the optimal number of states is unknown. This can be estimated by balancing model complexity and how well the model describes the data (fit quality). A measure designed to balance these is the Bayesian information criterion (BIC) [26], best measured on held-out data. We trained multiple GHMMs with varying numbers of states (2 to 15) using a leave-one-subject-out cross-validation (LOOCV) approach, evaluating the BIC on the held-out subject to identify the optimal number of states. The optimal number of states was determined based on the point at which increases in state count no longer improved the median BIC.

Direct comparisons between the states derived and the labelled sleep stages are not trivial. First, the states derived from the models are not directly related to a particular canonical sleep stage by design, requiring the alignment of states to stages for this evaluation. Second, the number of states may differ from the number of stages, leading to cases where a stage does not have a representative state. We used a minimally supervised approach to link hidden states to known sleep stages. For each candidate hidden state in the training set, we identified the epoch with the highest posterior probability—representing the most “typical” instance of that state—for each training subject. We then recorded the corresponding manual sleep stage label for that epoch. The most frequently occurring label across subjects was assigned as the representative label for the state. This procedure required less than 0.6% of the labelled data at 30-second resolution and less than 0.2% at the 4-second resolution, substantially reducing manual labelling effort and enabling scalable use in future applications.

We then assessed how well GHMM-assigned labels aligned with manual annotations. To numerically quantify the label agreement at the 30-second scale, we computed accuracy and Cohen's Kappa (in a LOOCV); the analysis resulted in only four states; thus, we did not compute the state-wise metrics as in the linear SVM analysis.

We compared agreement on overnight measures derived from the GHMM, SVM, and YASA [22] approaches at a group level. We estimated the total sleep time (TST), sleep onset latency (SOL), wake after sleep onset (WASO), sleep efficiency (SE), and time spent in each stage, with the corresponding measures obtained from manual hypnograms. We then computed inter-class correlation coefficients (ICCs),²⁷ and p-values to evaluate how consistently the measures in each approach aligned with the manual sleep scoring.

To better understand how GHMM states relate to canonical stages, we trained a unified model using the data from all subjects. First, we visualised the proportion of overlap between each GHMM state and conventional stage labels. Second, we plotted the temporal distribution of each state across a normalised night. Third, we examined the transition probability matrix between states and canonical stages. Finally, we created feature maps for both hidden states and canonical stages. For each hidden state, we averaged the z-scored spectral, EMG, EOG, and ECG features of the top 1% most prototypical epochs (posterior > 0.99 or top 99% quantile); we used all labelled epochs for sleep stage maps. These maps highlight the distinct spectral and physiological profiles of GHMM states and allow for a direct comparison with traditional stage-based representations.

Results

Principal Component Analysis Reveals a Dominant Sleep Axis (Hypno-PC)

Applying PCA to 30-second spectral features (EEG, EOG, EMG, ECG) and retaining components that together explained 90% of the total variance yielded 63 principal components (PCs), of which five accounted for more than 2% each, together explaining 71.8% of the variance. The first principal component, PC1 (“Hypno-PC”) alone explained 41.8% and faithfully tracked the hypnogram (Fig. 1A) as previously described [11]. However, its trajectory slid smoothly into deep NREM but shifted abruptly into REM or wake, aligning with models that treat NREM depth as continuous and REM/wake switches as threshold events [15,14,28].

Spatial-spectral maps (Fig. 1B) clarified the physiology: Hypno-PC is driven by high-frequency power, mainly alpha and beta, and a flattened spectral slope in the positive direction and by delta/slow-wave activity in the negative direction. Thus, the clustering of wake, REM, and N1 toward positive values and N2/N3 toward negative values (Fig. 1C) aligns well with previously described sleep physiology [29–31]. Mixed-effects modelling confirmed significant, subject-consistent stage effects for PC1, validating this as a quantitative marker of sleep depth across subjects (Fig. 1D).

PC1 Structure Persists Across Temporal and Spatial Resolutions

At the 4-second resolution, the first PC continued to track the hypnogram (Fig. S1), but within-stage variability increased, revealing microstate fluctuations and greater noise sensitivity. Still, PC1 retained the same stage gradient—wake and REM aligned with positive values and N2 and N3 with negative values.

A similar structure emerged using a standard six-electrode PSG montage (F3, F4, C3, C4, O1, O2; Fig.S2). Despite the lower spatial resolution, the PC1 profile preserved its characteristic polarity across stages.

Supervised Separability Analysis in the PC Space

The subsequent PCs captured additional dimensions of sleep-related variability. Fig. 1E shows how the canonical sleep stages cluster in this three-dimensional space (PC1-3). To evaluate the linear separability of conventional sleep stages in the PCA-transformed space, we trained a linear SVM classifier on increasing principal components using a leave-one-subject-out cross-validation strategy (LOOCV). This analysis was performed in the complete high-density electrode montage, in a reduced six-electrode configuration, and on the ICA space. Classification performance was benchmarked against the YASA algorithm [22], which was evaluated with the recommended EEG, EOG, EMG derivations, and subject demographics (age, sex).

Across both montages, increasing the number of PCs improved classification performance, as reflected in higher accuracy and Cohen's Kappa. The best results were achieved when using the complete set of PCs required to explain 90% of the variance. The most pronounced improvements were seen in challenging stages such as N1 and REM, where precision, recall, and F1-score increased substantially when moving from 5 to 63 components (or 22 in the six-electrode version; Figs. 1 and S2-3).

With only a single principal component, stage separability was below YASA performance across all tested configurations, and neither PC1 nor IC1 could reliably distinguish REM from N1, although IC1 achieved the best single-component performance (Kappa = 0.513, accuracy = 0.649; Supplementary Table S1).

Increasing the number of components markedly improved performance. With around five principal components, our full-montage PCA-SVM matched or slightly surpassed YASA's performance (Kappa = 0.687 vs 0.681, accuracy = 0.772 vs 0.763). Further incorporating all components accounting for 90% of the variance (63 PCs) enhanced classification performance substantially, reaching Kappa = 0.762 and accuracy = 0.826, with F1-scores for all individual stages surpassing the YASA benchmark. Similarly, the reduced six-electrode montage improved from Kappa = 0.675 and accuracy = 0.763 (5 PCs) to Kappa = 0.717 and accuracy = 0.795 when all 22 PCs (capturing 90% variance) were included.

These improvements were also evident in overnight metrics derived from classified hypnograms. The full-montage model (63 PCs) showed excellent agreement with manual scoring, outperforming YASA for total sleep time ($ICC = 0.967$), sleep onset latency ($ICC = 0.914$), wake after sleep onset ($ICC = 0.924$), and sleep efficiency ($ICC = 0.921$; Supplementary Table S2). The reduced montage (22 PCs) also maintained robust performance in total sleep time ($ICC = 0.963$) and sleep efficiency ($ICC = 0.915$), although it exhibited lower agreement for sleep onset latency ($ICC = 0.757$).

The Independent Components of Sleep

To further investigate the physiological processes underlying the low-dimensional PCA space, we applied ICA to the five major principal components. While PCA identifies orthogonal axes of maximal variance, ICA extracts statistically independent sources of variation, which do not need to be orthogonal. Applying PCA before ICA serves two purposes: it reduces the dimensionality of the feature space, removes near-zero variance components that can destabilise ICA, and improves numerical stability, facilitating reliable convergence. Although ICA is typically used on raw EEG to isolate short-lived artefacts or transient events [12], here, we applied it to the PCA-reduced space to identify stable, independent processes that span the entire night. Because both PCA and ICA are linear, their transformation weights can be used to visualise how each physiological feature contributes to a given independent component. Together with the component-time courses and their association with sleep stages, these spatial-spectral maps offer an interpretable view of the latent physiological generators shaping sleep architecture.

Figure. 2 presents a focused view of independent component (IC) 1, while Fig. S4 illustrates stage statistics and feature maps for ICs 2–5. The main findings for each IC are as follows:

- **IC1** is predominantly driven by fronto-central theta, posterior alpha, increased beta and gamma power, and spectral slope flattening, consistent with arousal-related physiology and REM sleep [30,31]. While slope flattening is also observed in PC1, IC1 offers more specific spatial and spectral activation patterns. It shows a stronger negative deflection during N2 than PC1.
- **IC2** is positively associated with theta and high sigma power and negatively associated with eye movements. It shows peak values and high variability during REM, N1, and N2, particularly in the second half of the night. This may reflect less stable processes during these stages, including changes in spindle density [32,31].
- **IC3** is characterised by positive weights in posterior alpha and low sigma power—features often linked to arousals [30] —and negative weights in delta power. It is most positive during wakefulness, consistently negative in N3, and near zero in the other stages.
- **IC4** is marked by increased EMG, EOG, and ECG activity, consistent with **active wakefulness**. Its time series shows short positive bursts corresponding to awakenings and mild but consistent negative values during N2–3. Its loading maps highlight fronto-central slow waves and elevated sigma and gamma activity, suggesting an association between these features and motor or arousal-related activity [30].

- **IC5** shows positive weights in frontal theta, alpha, beta, and gamma frequencies, increased entropy, high posterior power, and elevated EMG, HR, and HRV—features aligned with arousal [33]. In contrast, its negative weights reflect frontal slow waves, fronto-central theta, and lateral eye movements, characteristic of REM sleep [34]. This component appears to contrast REM and wake states.

These findings demonstrate how the current data-driven analysis can provide complementary and physiologically grounded insights. The analysis of the ICA-defined process unravels underlying sleep processes and may be useful for identifying altered sleep patterns in clinical contexts.

The Gaussian Hidden Markov Model (GHMM) States

Macrostate Architecture

Using the GHMM, we identified latent sleep states directly from PCA- and ICA-transformed electrophysiological data. We applied the BIC metric at a 30-second temporal resolution and determined that four states provided the best fit. These states closely aligned with canonical sleep stages (Fig. 3A): state 0 corresponded chiefly to wake, state 1 matched N2, state 2 reflected N3 and State 3 combined REM and N1. This four-state solution replicated across PCA and ICA representations, yielding nearly identical state profiles and transition patterns at this resolution (see Fig. S12). Labels assigned with minimal supervision showed strong concordance with manual scoring (Cohen's Kappa = 0.701, accuracy = 0.781), closely matching the YASA benchmark (Supplementary Table S1). For overnight metrics that depend on the wake-sleep boundary (TST, WASO, SE), the GHMM outperformed YASA and was broadly equivalent to the 5-component SVM. Notably, GHMM produced the most accurate estimate of SOL, underscoring the value of temporal context for detecting sleep onset. Conversely, agreement on time spent at each stage was lower than for supervised methods, likely because the four-state model merges N1 with REM.

Feature Representation of GHMM States

Feature maps (Figure 3D) revealed distinct spectral and physiological signatures, while canonical stage maps (Fig. S8) provided context. Several key findings were observed in these maps:

- State 0 (Wake): Elevated spectral slope, posterior alpha, gamma, EMG, and HR, associated with the waking state [30,33].
- State 3 (REM/N1): Prominent central theta and beta and posterior gamma activity, more like the REM map (Fig. S8), matching earlier descriptions [34]
- State 1 (N2): Strong bilateral mid-parietal sigma activity, representing spindle activity [32]
- State 2 (N3): Dominant slow-wave activity with a steep negative spectral slope [29]

Temporal and Transition Dynamics

Fig. 3B shows high self-transition probabilities (state stability) and strongly imbalanced bidirectional edges, reproducing the asymmetry reported by Lo et al. 2013 [35]. No direct transitions between the deep-sleep state (N3) and REM sleep were observed. Deep-sleep epochs always passed through lighter NREM or a brief wake state before REM, mirroring canonical hypnograms³⁶ and intermediate-state evidence [37,38].

The wake-like state (State 0) showed the lowest self-stability of the four macrostates—an outcome expected during nocturnal sleep, when homeostatic and circadian pressures pull the system toward sleep [39]. Transitions from State 0 led mainly to the REM- and N2-like states and only rarely to N3. In line with classical sleep architecture, the nightly profile revealed an early dominance of the N3-like state with clear cycles, followed by a steady rise in N2- and REM-like occupancy as the night progressed (Fig. 3C), mirroring canonical hypnogram patterns [36]. Wake-like states did not show any systematic trend.

Microstate Architecture

Applying GHMM to 4-second ICA data yielded 11 microstates (Figs. 4–6). On this scale, only 58.2% of possible edges were present (vs. 83.3% for macrostates), and 78.1% were bi-directional (Supplementary Table S5), highlighting more specific transition dynamics. Microstates clustered into three functional families: REM-related, Wake-related, and NREM-related.

Wake-related microstates (States 5, 6, 10)

States 5 and 6 represent **quiet wake** with minimal peripheral activation. State 5 shows high posterior alpha, while state 6 exhibits global alpha, consistent with eyes-closed relaxed wakefulness [40] and alpha reactivity during nocturnal arousals [33]. State 5 occurs mainly at sleep-bout edges, whereas state 6 appears sporadically throughout the night. State 10, **active wake**, displays elevated EMG, EOG, HR, and widespread gamma, characteristic of alert wakefulness [41]. Moreover, state 10 is a network hub (in-degree = 10, out-degree = 9) with the lowest self-stability in the wake states, supporting its role as a transient bridge state.

NREM-related microstates (States 0, 2–4, 8, 9)

Spindle-rich N2 states (0 & 8) show focal sigma bursts; their prevalence rises overnight, matching the well-known increase in spindle density [32]. **Slow-wave-dominant** states (2–4) feature strong delta and steep slopes. States 2 and 3 are confined to early cycles, whereas state 4 becomes common later and acts as a hub (in-degree=7, out-degree=6), supporting its role as a transition state. Further, the low state stability compared to the other slow-wave-dominant states may reflect the declining pressure to generate slow-wave activity (SWA) [29]. State 9 resembles N1: shallow slope, elevated beta, reduced delta. Its high hubness (indegree = 7, outdegree = 7), low stability, and edge pattern suggest a transitional role among N1, wake, and REM.

REM-related microstates (States 1 & 7).

State 1 exhibits posterior gamma and fronto-central theta with strong EOG bursts, which are characteristics of **phasic REM**. State 7 shows diffuse theta-beta with no eye movements, which are characteristics of **tonic REM** [34]. State 1 overlaps mostly with REM epochs, while state 7 is split between REM, N1, and N2. Both peak in the second half of the night. State 1 is entered from N1-like (9), tonic REM (7), or wake (10/5/6); state 7 is reached mainly from N1 (9), phasic REM (1), late slow-wave (4), or active Wake (10).

PCA microstates

A parallel GHMM on 4-s PCA data selected **seven** microstates (Figs S9–S11). While capturing the main distinctions (active vs. quiet wake, N1, spindle-rich, slow-wave, single REM), it did **not** separate phasic versus tonic REM or the two quiet-wake forms. This difference implies that the ICA space better disentangles these subtle states and that BIC alone may underestimate the needed state count in PCA space.

Discussion

Sleep is often presented as a tidy sequence of five 30-s labels, yet recent research [28,15,14,11] and the results of the current work confirm that the brain follows a far richer and more fluid script. By combining fully linear embeddings with explicit temporal modelling, we bridged the gap between the established clinical stages and the continuous, region-specific, and temporal dynamics apparent in high-density PSG.

A continuous axis of sleep depth

The first principal component—Hypno-PC—captured 42 % of spectral-autonomic variance and reproduced the hypnogram without supervision. The fact that this axis emerges from a fully unsupervised, linear decomposition of high-density EEG—and is reproducible even when using a reduced six-electrode subset—demonstrates its robustness. Furthermore, its convergence with findings from sparse-montage studies [11] supports the idea that a single, interpretable dimension can capture the dominant structure of a full night of sleep. Nevertheless, Hypno-PC emphasised two important twists: (i) the descent from light to deep NREM appears as a smooth glide rather than a ladder of discrete rungs, and (ii) switches into REM or wake stages manifest as abrupt leaps, underscoring the asymmetric dynamics of sleep-wake control [14,15].

From spectra to physiology: ICA reveals latent generators

Because the Hypno-PC is inherently global and sleep physiology is multifaceted, additional dimensions are needed to distinguish the parallel processes that unfold throughout the night. Our supervised analysis confirms that including extra principal components markedly improves stage separability, highlighting the information carried by these additional dimensions. Still, the strict orthogonality of PCA can blur truly independent generators, making the raw PC space sub-optimal. Relaxing this constraint with independent-component analysis [42] allowed us to isolate spindle-rich, slow-wave-dominant, and arousal-related sources, tying the embedding back to recognisable thalamocortical and brain-stem circuits by identifying key oscillatory patterns [29,32]. Such physiological transparency is far harder to recover from more powerful but opaque nonlinear manifolds [8,43]. However, the oscillation state maps we developed can be applied to any model that provides state assignments, as long as electrophysiological recordings are included.

Temporal script uncovered by a GHMM

Embedding alone cannot reveal how the sleeping brain moves through state space. To capture this temporal dimension, we trained a GHMM on the ICA features, combining each epoch's spectral "fingerprint" with the transition context provided by its neighbours [13]. At the conventional 30-s granularity, the GHMM recovered four macrostates that corresponded closely to wake, a combined N1/REM state, N2, and N3, achieving Cohen's Kappa = 0.70 while using < 1 % of labelled epochs solely to assign state names—delivering the most accurate sleep-onset latency among the automated methods we evaluated. When the window was shortened to 4 seconds, the same model resolved 11 microstates that teased apart tonic versus phasic REM, active versus quiet wakefulness, spindle versus slow-wave-dominant NREM, and an N1-like gateway state, composing a fast-cycling repertoire closely reminiscent of the cyclic alternating pattern (CAP) that indexes sleep instability [44].

Three of these microstates acted as network hubs:

- An active wake state with a combination of gamma activity, slow waves, and peripheral activation.
- An N1-like state, characterised by elevated high frequencies and mainly beta power.
- A late-night slow-wave state that overlapped chiefly with N2 epochs.

Together, these microstates mediated the majority of micro-to-micro transfers. At both temporal resolutions, the resulting transition matrices produced the strong directional asymmetry previously reported for sleep-stage pathways [35] and confirmed the near-absence of direct N3 ↔ REM jumps, consistent with models that posit obligatory intermediary states [45]. These probabilistic pathways offer compact, quantitative sleep continuity and fragmentation markers [46].

Clinical and translational relevance

The present pipeline was developed with healthy sleepers, yet its explicit linkage between latent axes and concrete spectral-spatial features makes it well-suited for clinical translation. Because every PCA- or ICA-derived dimension is an explicit weighted sum of frequencies and channels, and every GHMM is linked to a state map, abnormal dynamics can be traced directly to recognisable oscillations or cortical regions.

Insomnia. Maintenance insomnia is characterised by frequent intrusions of wakefulness and unstable NREM continuity. In our framework, this is expected to appear as (i) reduced self-stability of N2/N3 microstates, (ii) inflated transition probabilities into wake-like hubs, and (iii) a smaller separation between Wake and NREM along the Hypno-PC axis, potentially reflecting impaired mutual inhibition within the sleep-switch circuitry [45]. Microstates that consistently precede clinical arousals could be isolated, and their spectra could be compared with high-density EEG findings in insomnia [47,48], providing a quantitative marker of hyper-arousal severity.

Obstructive sleep apnea. OSA elicits brief cortical arousals tightly coupled to respiratory and autonomic bursts [49]. Our ICA layer already isolates an arousal-related component rich in gamma, EMG, and tachycardia; an increased dwell time in or higher transition probability toward this microstate could serve as an objective index of respiratory disturbance [4]. Comparing the spectral fingerprints of apnea-linked states with normative templates may disentangle neural from autonomic contributors to sleep fragmentation.

Narcolepsy. A defining biomarker is the abrupt passage from wake directly into REM [38]. Such shortcuts should manifest in our transition matrix as high-probability wake → REM edges that bypass the N1 gateway. The 4-s model further allows us to examine whether tonic- or phasic-REM microstates dominate these pathological transitions, potentially distinguishing narcolepsy Type 1 from Type 2 [50].

REM sleep behaviour disorder (RBD). Healthy phasic REM is accompanied by a frontal beta reduction that is blunted in RBD [51]. As our REM microstates separate tonic and phasic sub-modes, the persistence of beta-rich tonic-like states during nominal phasic epochs, or REM-labelled states retaining elevated EMG could, thus, provide an electrophysiological fingerprint of RBD [52,53].

Epilepsy. Seizure expression is tightly interwoven with sleep physiology [54,55], and patients are often monitored continuously for days or weeks—an ideal setting for our framework. Tracking high-resolution microstates across these long recordings, the PCA → ICA → GHMM pipeline could identify latent patterns that reliably precede seizures [56], quantify transition probabilities into pro-ictal states, and compare these trajectories with normative sleep-wake dynamics. Estimating how far and quickly the brain deviates from typical pathways may enable earlier warnings and more accurate forecasts. Because our model operates at multiple timescales, it can capture both slow build-ups and rapid pre-ictal shifts, and its explicit feature weights facilitate integration with multimodal seizure detection systems.

Together, these vignettes illustrate how a single, interpretable framework can map disorder-specific alterations where the brain sits within spectral-spatial space and how it traverses that space over time, paving the way for objective biomarkers and personalised therapeutic targets.

Limitations and future directions

Although the present pipeline provides a transparent view of sleep dynamics, several methodological choices constrain its current scope.

Fixed-length windows. All analyses were performed on pre-segmented 30- and 4-s epochs. Sleep, however, is not obliged to respect these artificial boundaries. Data-driven change-point or segmentation algorithms could adapt the window length to the signal itself and may reveal additional micro states or transition motifs that straddle conventional epoch borders [57].

Emission model simplicity. We modelled each latent state with a single multivariate Gaussian for parsimony. However, the IC distribution of microstates may not be well represented as such. Gaussian-mixture or semi-Markov formulations could capture such heterogeneity and improve the resolution of rare or transient states.

Selecting the number of states. The Bayesian information criterion offered an objective starting point, yet physiology, not statistics alone, should guide the final choice. Future work should balance information criteria with domain-specific priors and explore hierarchical models that allow the state cardinality to vary across time-scales or clinical conditions.

Richer feature sets. This work focused mainly on spectral features, but raw EEG, metrics of critical brain dynamics [58,59], functional connectivity [60], and nonneural signals (respiratory effort, oxygen saturation, hemodynamics) [61] could provide complementary views, especially in cardiorespiratory disorders. Integrating multi-modal data within the same linear-temporal framework is a natural next step.

Generalisability. The cohort comprised 29 healthy adults. Replication in larger and more diverse populations and patient groups is essential to test robustness, uncover disorder-specific microstates, and examine how recording density or wearable sensors affect performance [62].

Addressing the above limitations will sharpen the physiological specificity of the latent states, extend the method beyond the sleep laboratory, and accelerate its translation into clinical-decision support.

Conclusion

Our fully linear, minimally supervised pipeline—combining PCA, ICA, and a temporally explicit GHMM—bridges traditional 30-s stage scoring with the continuous, fine-grained dynamics of sleep. It reliably recovers canonical stages and reveals physiologically interpretable microstates while retaining direct links to spectral features that clinicians understand. This transparency positions the approach as a scalable foundation for objective sleep phenotyping across healthy and clinical populations and as a springboard for future multimodal, home-based, and personalised sleep analytics.

Acknowledgements

We want to acknowledge Prof. Yuval Nir for his advice and suggestions on following this direction. We also acknowledge Prof. Christoph Bernard for reviewing the original manuscript and providing invaluable input.

Funding

This research was supported by Israel Science Foundation grant 794/22 to O.S.

Disclosure Statement

Financial Disclosure: none

Nonfinancial Disclosure: none

Data availability

We used the ANPHY-Sleep database [16] for the analysis presented in this study. This database is publicly available and can be accessed through <https://doi.org/10.17605/OSF.IO/R26FH>.

Code availability

The code repository will be made available upon publication via GitHub:

https://github.com/miriamguen/high_density_sleep.git

References

1. Troester MM, Quan SF, American Academy of Sleep Medicine, Berry RB. *The AASM Manual for the Scoring of Sleep and Associated Events, Version 3*: American Academy Of Sleep Medicine; 2023.
2. Brown RE, Basheer R, McKenna JT, Strecker RE, McCarley RW. Control of sleep and wakefulness. *Physiol Rev* 2012;92(3):1087-1187. doi:10.1152/physrev.00032.2011.
3. Stein PK, Pu Y. Heart rate variability, sleep and sleep disorders. *Sleep Med Rev* 2012;16(1):47-66. doi:10.1016/j.smrv.2011.02.005.
4. Jones SG, Riedner BA, Smith RF et al. Regional reductions in sleep electroencephalography power in obstructive sleep apnea: a high-density EEG study. *Sleep* 2014;37(2):399-407. doi:10.5665/sleep.3424.

5. Amato N, Caverzasio S, Galati S. Clinical implication of high-density EEG sleep recordings in Parkinson's disease. *J Neurosci Methods* 2020;340:108746. doi:10.1016/j.jneumeth.2020.108746.
6. Lustenberger C, Huber R. High density electroencephalography in sleep research: potential, problems, future perspective. *Front Neurol* 2012;3:77. doi:10.3389/fneur.2012.00077.
7. Cunningham JP, Yu BM. Dimensionality reduction for large-scale neural recordings. *Nat Neurosci* 2014;17(11):1500-1509. doi:10.1038/nn.3776.
8. Rué-Queralt J, Stevner A, Tagliazucchi E et al. Decoding brain states on the intrinsic manifold of human brain dynamics across wakefulness and sleep. *Commun Biol* 2021;4(1):854. doi:10.1038/s42003-021-02369-7.
9. Yang FN, Picchioni D, Zwart JA de, Wang Y, van Gelderen P, Duyn JH. Reproducible, data-driven characterisation of sleep based on brain dynamics and transitions from whole-night fMRI. *Elife* 2024;13. doi:10.7554/eLife.98739.
10. Pearson K. LIII. On lines and planes of closest fit to systems of points in space. *The London, Edinburgh, and Dublin Philosophical Magazine and Journal of Science* 1901;2(11):559-572. doi:10.1080/14786440109462720.
11. Metzner C, Schilling A, Traxdorf M, Schulze H, Tziridis K, Krauss P. Extracting continuous sleep depth from EEG data without machine learning. *Neurobiol Sleep Circadian Rhythms* 2023;14:100097. doi:10.1016/j.nbscr.2023.100097.

12. Makeig S, Bell A, Jung T-P, SEJNOWSKI TJ. Independent Component Analysis of Electroencephalographic Data. In: D. Touretzky, M.C. Mozer, M. Hasselmo, eds. Advances in Neural Information Processing Systems. Vol. 8: MIT Press; 1995.
13. Rabiner LR. A tutorial on hidden Markov models and selected applications in speech recognition. Proc. IEEE 1989;77(2):257-286. doi:10.1109/5.18626.
14. Dvir H, Kantelhardt JW, Zinkhan M et al. A Biased Diffusion Approach to Sleep Dynamics Reveals Neuronal Characteristics. Biophys J 2019;117(5):987-997. doi:10.1016/j.bpj.2019.07.032.
15. Lo C-C, Amaral LAN, Havlin S et al. Dynamics of sleep-wake transitions during sleep. Europhys Lett 2002;57(5):625-631. doi:10.1209/epl/i2002-00508-7.
16. Wei X, Avigdor T, Ho A et al. ANPHY-sleep: an open sleep database from healthy adults using high-density scalp Electroencephalogram. Sci Data 2024;11(1):896. doi:10.1038/s41597-024-03722-1.
17. Gramfort A, Luessi M, Larson E et al. MEG and EEG data analysis with MNE-Python. Front Neurosci 2013;7:267. doi:10.3389/fnins.2013.00267.
18. Shaffer F, Ginsberg JP. An Overview of Heart Rate Variability Metrics and Norms. Front Public Health 2017;5:258. doi:10.3389/fpubh.2017.00258.
19. Virtanen P, Gommers R, Oliphant TE et al. SciPy 1.0: fundamental algorithms for scientific computing in Python. Nat Methods 2020;17(3):261-272. doi:10.1038/s41592-019-0686-2.

20. Penzel T, Kantelhardt JW, Bartsch RP et al. Modulations of Heart Rate, ECG, and Cardio-Respiratory Coupling Observed in Polysomnography. *Front Physiol* 2016;7:460. doi:10.3389/fphys.2016.00460.
21. Seabold S, Perktold J. Statsmodels: Econometric and Statistical Modeling with Python. In: Stéfan van der Walt, Jarrod Millman, eds. *Proceedings of the 9th Python in Science Conference*; 2010:92-96.
22. Vallat R, Walker MP. An open-source, high-performance tool for automated sleep staging. *eLife* 2021;10. doi:10.7554/eLife.70092.
23. Ablin P, Cardoso J-F, Gramfort A. Faster independent component analysis by preconditioning with hessian approximations. *IEEE TSP* 2018;66(15):4040-4049. doi:10.1109/TSP.2018.2844203.
24. Vyazovskiy VV, Tobler I. The temporal structure of behaviour and sleep homeostasis. *PLoS One* 2012;7(12):e50677. doi:10.1371/journal.pone.0050677.
25. Bilmes JA. A gentle tutorial of the EM algorithm and its application to parameter estimation for Gaussian mixture and hidden Markov models. *International computer science institute* 1998;4(510):126.
26. Schwarz G. Estimating the Dimension of a Model. *Ann. Statist.* 1978;6(2). doi:10.1214/aos/1176344136.

27. Stepnowsky C, Levendowski D, Popovic D, Ayappa I, Rapoport DM. Scoring accuracy of automated sleep staging from a bipolar electroocular recording compared to manual scoring by multiple raters. *Sleep Med* 2013;14(11):1199-1207.
doi:10.1016/j.sleep.2013.04.022.
28. Schulz H. Rethinking Sleep Analysis. *J Clin Sleep Med* 2008;04(02):99-103.
doi:10.5664/jcsm.27124.
29. Riedner BA, Vyazovskiy VV, Huber R et al. Sleep homeostasis and cortical synchronisation: III. A high-density EEG study of sleep slow waves in humans. *Sleep* 2007;30(12):1643-1657.
doi:10.1093/sleep/30.12.1643.
30. Schwabedal JTC, Riedl M, Penzel T, Wessel N. Alpha-wave frequency characteristics in health and insomnia during sleep. *J Sleep Res* 2016;25(3):278-286. doi:10.1111/jsr.12372.
31. Siclari F, Baird B, Perogamvros L et al. The neural correlates of dreaming. *Nat Neurosci* 2017;20(6):872-878. doi:10.1038/nn.4545.
32. Fernandez LMJ, Lüthi A. Sleep Spindles: Mechanisms and Functions. *Physiol Rev* 2020;100(2):805-868. doi:10.1152/physrev.00042.2018.
33. Halász P, Terzano M, Parrino L, Bódizs R. The nature of arousal in sleep. *J Sleep Res* 2004;13(1):1-23. doi:10.1111/j.1365-2869.2004.00388.x.
34. Simor P, van der Wijk G, Nobili L, Peigneux P. The microstructure of REM sleep: Why phasic and tonic? *Sleep Med Rev* 2020;52:101305. doi:10.1016/j.smrv.2020.101305.

35. Lo C-C, Bartsch RP, Ivanov PC. Asymmetry and Basic Pathways in Sleep-Stage Transitions. *Europhys Lett* 2013;102(1):10008. doi:10.1209/0295-5075/102/10008.
36. Carskadon MA, Dement WC. Normal Human Sleep. In: *Principles and Practice of Sleep Medicine*: Elsevier; 2017:15-24.e3.
37. Carrera-Cañas C, Garzón M, Andrés I de. The Transition Between Slow-Wave Sleep and REM Sleep Constitutes an Independent Sleep Stage Organized by Cholinergic Mechanisms in the Rostrodorsal Pontine Tegmentum. *Front Neurosci* 2019;13:748. doi:10.3389/fnins.2019.00748.
38. Liu Y, Zhang J, Lam V et al. Altered Sleep Stage Transitions of REM Sleep: A Novel and Stable Biomarker of Narcolepsy. *J Clin Sleep Med* 2015;11(8):885-894. doi:10.5664/jcsm.4940.
39. Saper CB, Chou TC, Scammell TE. The sleep switch: hypothalamic control of sleep and wakefulness. *TINS* 2001;24(12):726-731. doi:10.1016/s0166-2236(00)02002-6.
40. Barry RJ, Clarke AR, Johnstone SJ, Brown CR. EEG differences in children between eyes-closed and eyes-open resting conditions. *Clin Neurophysiol* 2009;120(10):1806-1811. doi:10.1016/j.clinph.2009.08.006.
41. Boytsova YA, Danko SG. EEG differences between resting states with eyes open and closed in darkness. *Hum Physiol* 2010;36(3):367-369. doi:10.1134/S0362119710030199.

42. Bell AJ, Sejnowski TJ. An information-maximisation approach to blind separation and blind deconvolution. *Neural Comput* 1995;7(6):1129-1159. doi:10.1162/neco.1995.7.6.1129.
43. Yang FN, Picchioni D, Zwart JA de, Wang Y, van Gelderen P, Duyn JH. *Reproducible, data-driven characterisation of sleep based on brain dynamics and transitions from whole-night fMRI*; 2024. doi.org/10.7554/eLife.98739
44. Parrino L, Ferri R, Bruni O, Terzano MG. Cyclic alternating pattern (CAP): the marker of sleep instability. *Sleep Med Rev* 2012;16(1):27-45. doi:10.1016/j.smrv.2011.02.003.
45. Saper CB, Fuller PM, Pedersen NP, Lu J, Scammell TE. Sleep state switching. *Neuron* 2010;68(6):1023-1042. doi:10.1016/j.neuron.2010.11.032.
46. Laffan A, Caffo B, Swihart BJ, Punjabi NM. Utility of sleep stage transitions in assessing sleep continuity. *Sleep* 2010;33(12):1681-1686. doi:10.1093/sleep/33.12.1681.
47. Wei Y, Colombo MA, Ramautar JR et al. Sleep Stage Transition Dynamics Reveal Specific Stage 2 Vulnerability in Insomnia. *Sleep* 2017;40(9). doi:10.1093/sleep/zsx117.
48. Feige B, Baglioni C, Spiegelhalder K, Hirscher V, Nissen C, Riemann D. The microstructure of sleep in primary insomnia: an overview and extension. *Int J Psychophysiol* 2013;89(2):171-180. doi:10.1016/j.ijpsycho.2013.04.002.
49. Berry RB, Brooks R, Gamaldo C et al. AASM scoring manual updates for 2017 (Version 2.4). *J Clin Sleep Med* 2017;13(5):665-666. doi:10.5664/jcsm.6576.

50. Thorpy MJ, Siegel JM, Dauvilliers Y. REM sleep in narcolepsy. *Sleep Med Rev* 2024;77:101976. doi:10.1016/j.smrv.2024.101976.
51. Valomon A, Riedner BA, Jones SG et al. A high-density electroencephalography study reveals abnormal sleep homeostasis in patients with rapid eye movement sleep behavior disorder. *Sci Rep* 2021;11(1):4758. doi:10.1038/s41598-021-83980-w.
52. Ferri R, Manconi M, Plazzi G et al. A quantitative statistical analysis of the submentalis muscle EMG amplitude during sleep in normal controls and patients with REM sleep behavior disorder. *J Sleep Res* 2008;17(1):89-100. doi:10.1111/j.1365-2869.2008.00631.x.
53. Figorilli M, Lanza G, Congiu P et al. Neurophysiological aspects of REM sleep behavior disorder (RBD): a narrative review. *Brain Sci* 2021;11(12). doi:10.3390/brainsci11121588.
54. Bernard C, Frauscher B, Gelinas J, Timofeev I. Sleep, oscillations, and epilepsy. *Epilepsia* 2023;64 Suppl 3(Suppl 3):S3-S12. doi:10.1111/epi.17664.
55. Sheybani L, Frauscher B, Bernard C, Walker MC. Mechanistic insights into the interaction between epilepsy and sleep. *Nat Rev Neurol* 2025;21(4):177-192. doi:10.1038/s41582-025-01064-z.
56. Ilyas A, Alamoudi OA, Riley KO, Pati S. Pro-Ictal State in Human Temporal Lobe Epilepsy. *NEJM Evid* 2023;2(3):EVIDoa2200187. doi:10.1056/EVIDoa2200187.
57. Truong C, Oudre L, Vayatis N. Selective review of offline change point detection methods. *Signal Processing* 2020;167:107299. doi:10.1016/j.sigpro.2019.107299.

58. Fekete T, Hinrichs H, Sitt JD, Heinze H-J, Shriki O. Multiscale criticality measures as general-purpose gauges of proper brain function. *Sci Rep* 2021;11(1):14441. doi:10.1038/s41598-021-93880-8.
59. Zimmern V. Why Brain Criticality Is Clinically Relevant: A Scoping Review. *Front Neural Circuits* 2020;14:54. doi:10.3389/fncir.2020.00054.
60. Chiari G, Sparacino L, Antonacci Y, Faes L, Mesin L. Connectivity analysis in EEG data: a tutorial review of the state of the art and emerging trends. *Bioengineering (Basel)* 2023;10(3). doi:10.3390/bioengineering10030372.
61. Klimesch W. The frequency architecture of brain and brain body oscillations: an analysis. *Eur J Neurosci* 2018;48(7):2431-2453. doi:10.1111/ejn.14192.
62. Ma YJX, Zschocke J, Glos M et al. Automatic sleep-stage classification of heart rate and actigraphy data using deep and transfer learning approaches. *Comput Biol Med* 2023;163:107193. doi:10.1016/j.combiomed.2023.107193.

Figures

Graphical abstract

Top Panel: Schematic overview of our analysis pipeline. High-density EEG, EOG, EMG, and ECG recordings are converted into modality-specific spectral and physiological features. Principal-component analysis (PCA) compresses this high-dimensional feature space, and independent-component analysis (ICA) is then applied to the leading PCs to disentangle partially independent physiological processes. **Middle Panel:** *Left:* a 3-D embedding (first three PCs) locates each 30-s epoch within a continuous state-space, revealing how stages cluster and merge. *Centre:* The time series of the dominant PCs/ICs are plotted beneath the manual hypnogram, with gradual drifts into deep NREM in contrast with the sharp switches characterizing REM or brief awakenings. *Right:* filter (loading) maps show how original spectral features contribute to each component, linking abstract axes to spatial and frequency-specific physiology. **Bottom Panel:** Discrete state analysis was performed in the PCA/ICA space. *Supervised:* a linear SVM, evaluated with leave-one-out cross-validation, quantifies how well conventional AASM stages can be separated in PCA/ICA space, and its performance is benchmarked against YASA [22] on both the complete high-density montage and a standard six-electrode set (F3, F4, C3, C4, O1, O2). *Unsupervised:* a Gaussian Hidden Markov Model (GHMM) fitted to the ICA space discovers data-driven states. We report the optimal number of states, their overnight prevalence, transition matrices, and mean feature maps at both 30-s and 4-s resolutions and examine the resulting states/microstates in the context of traditional sleep staging.

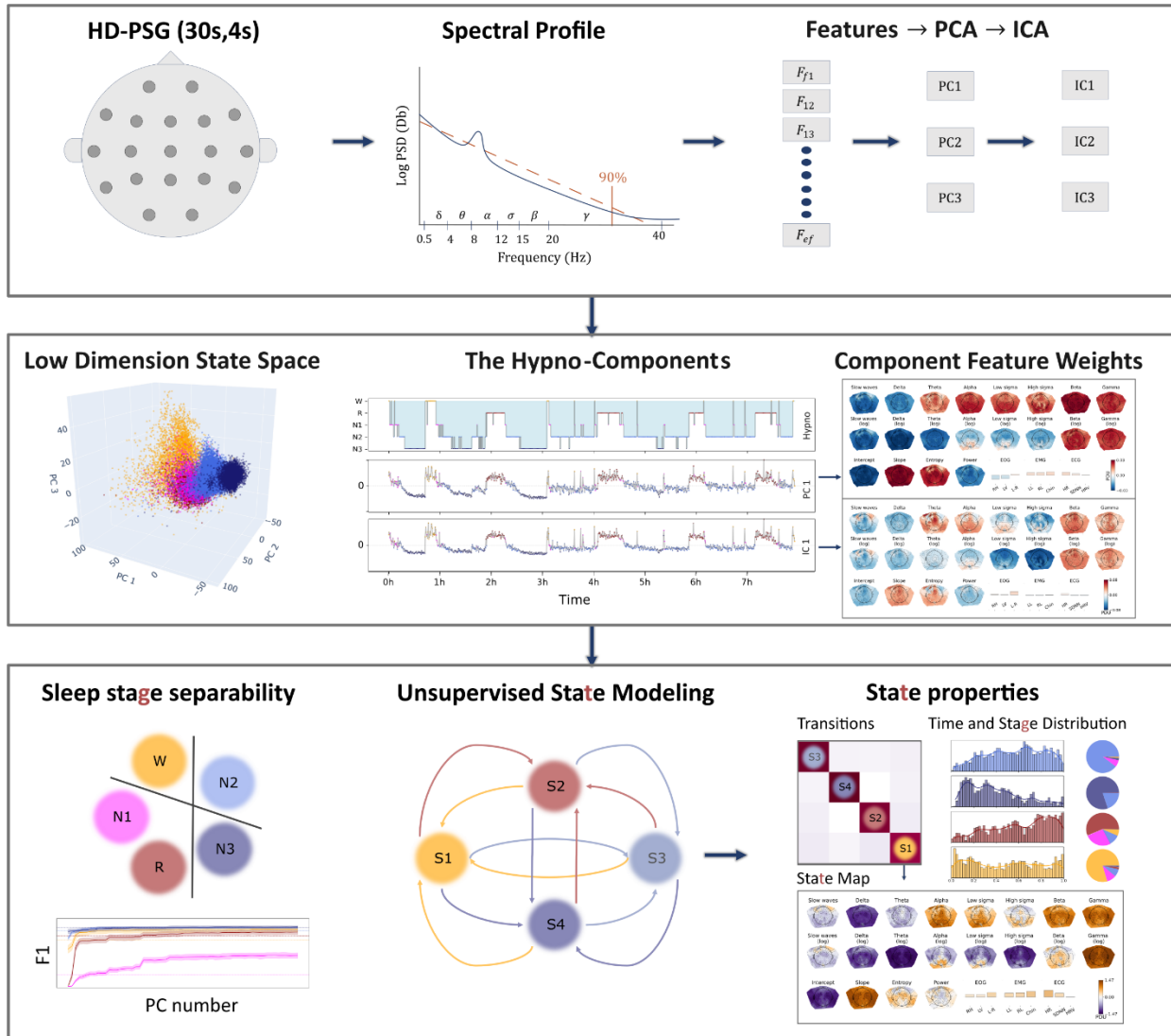


Figure 1 - Hypno-PC and low-dimensional sleep stage representation.

- (a) **Hypnogram vs. Hypno-PC.** The upper trace shows the manually scored hypnogram; the lower trace depicts the first principal component (PC1, “Hypno-PC”) extracted from high-density EEG, EOG, EMG, and ECG features. PC1 closely aligns with the hypnogram and attains high positive values during wake and REM sleep and low values during N3. The descent into deep NREM is continuous, bypassing a discrete N2 plateau, whereas transitions from NREM to REM or wakefulness are abrupt.
- (b) **PC1 loading maps.** The red-blue scale denotes the sign and magnitude of each loading. Positive loadings (red) push the component towards higher values, which predominate during wakefulness and REM sleep; negative loadings (blue) pull the component towards lower values, characteristic of NREM sleep, with the most negative values corresponding to deep N3. Thus, high-frequency activity is mapped to the positive end of PC1. In contrast, low-frequency activity is mapped to the negative end, reflecting the expected spectral contrast between wake/REM and slow-wave sleep.
- (c) **Stage-wise distribution of PC1 across participants.** The empirical distribution of PC1 values separates wakefulness from N2/N3. REM and N1 partially overlap, indicating that additional dimensions are required to disambiguate these stages.
- (d) **Cross-subject consistency of PC1.** A linear mixed-effects model, with sleep stage as a fixed effect and participant as a random effect, reveals consistent stage-dependent coefficients. The coloured dots and bars represent the mean and 95% CI of the model fit. The grey points denote participant-specific slopes, confirming uniform directionality across the cohort.
- (e) **Three-dimensional projection space (PCs 1–3).** Conventional stages cluster in the principal-component space, although N1 and REM remain partly confluent, mirroring panels C and D.
- (f) **Stage separability in the PCA space.** A linear support-vector machine, evaluated with leave-one-out cross-validation, shows progressively higher accuracy and Cohen’s K as additional PCs are included, matching the performance of the YASA algorithm [22] (dashed line) with approximately four to six components. Stage-specific F1 scores demonstrate that N1 and

REM remain the most challenging to classify, albeit with marked improvement as dimensionality increases.

Figs S1–S3 extend these comparisons by repeating the analysis with 4-s epochs and a conventional six-electrode PSG montage.

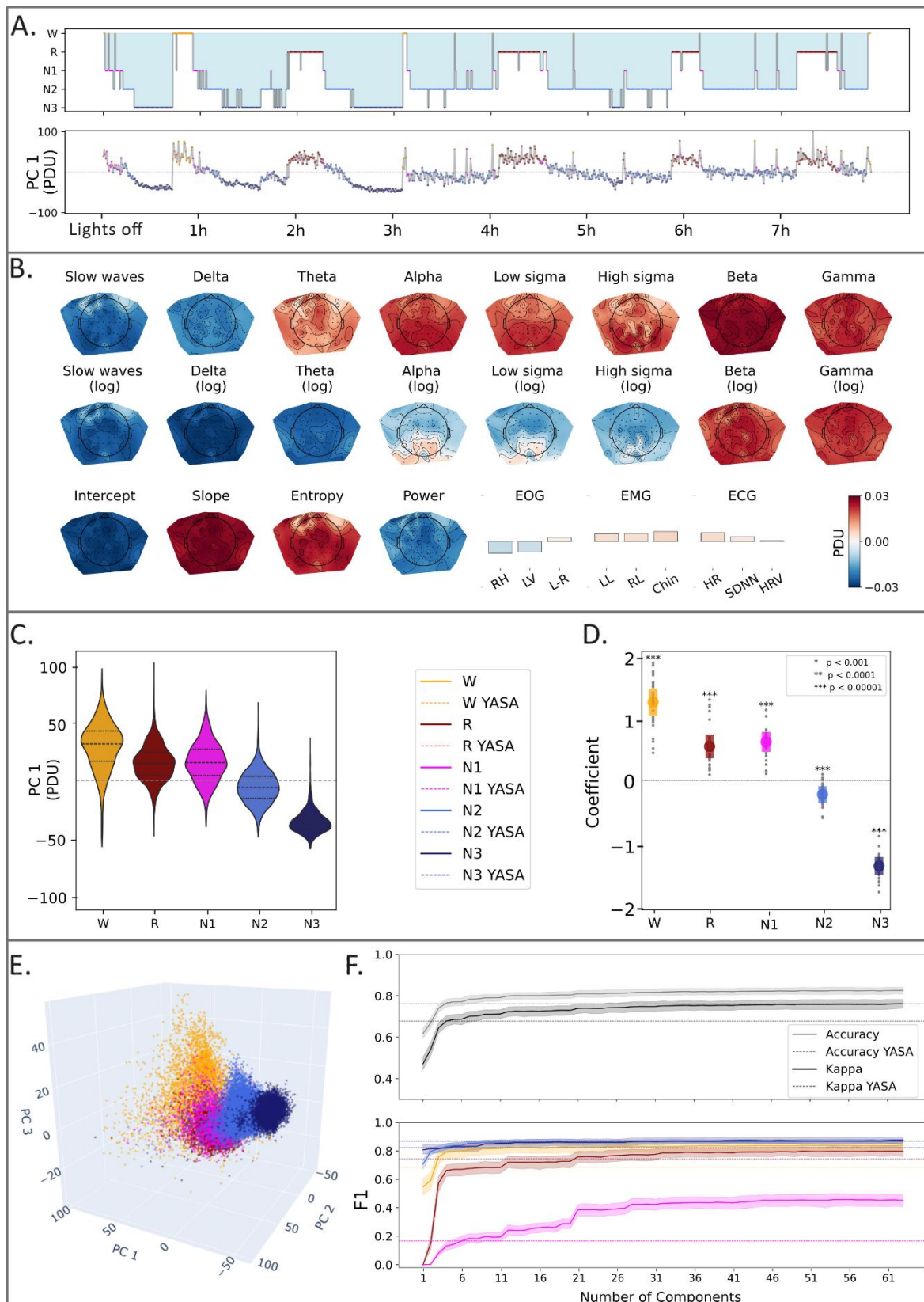


Figure 2 – Independent-component (IC) representation of sleep dynamics

(a) **Time-series overview.** The manually scored hypnogram is plotted above the five independent components (ICs) obtained by applying independent components analysis (ICA) to the first five principal components (PCs).

IC1 aligns closely with the hypnogram and shows an even stronger contrast than PC1 between wake/REM (positive values) and N2–N3 (negative values).

IC2 runs from negative values in N3 through N1/N2 to positive values in REM, reflecting the continuum between slow-wave and more activated states. It becomes more variable in the second half of the night and is dominated by theta and high-sigma activity (Fig. S4).

IC3 primarily differentiates wake from N3. Variability is most significant during wake, even though brief arousals are not strongly captured, suggesting a quiet, low-movement sub-state of wakefulness. This aligns well with the component loadings, driven mainly by alpha activity (Fig. S4).

IC4 emphasises an arousal-related process, showing brief positive surges that coincide with short awakenings. Its loadings include strong EMG, EOG, and ECG contributions, as well as high-sigma and gamma power (Fig. S4).

IC5 assigns positive values to wake and negative values to REM, with marked variability in both. Its loadings contrast frontal alpha/gamma, HR, and muscle activity (wake) with frontal slow waves, lateral eye movements, and posterior beta/sigma (REM) (Fig. S4).

(b) **Topographic feature-weight maps.** Illustrate how EEG electrode locations, frequency bands, and non-EEG measures (EOG, EMG, ECG) contribute to PC1. High positive weights appear in the posterior alpha, fronto-central theta, and high-frequency EEG signals. Markers that are typical of wakefulness. Negative weights for central posterior sigma and

slow waves are associated with N2/N3. Compared to PC1, IC1 shows a more specific spatial distribution, implying finer spatial feature discrimination.

- (c) ***Cross-subject distributions.*** IC 1 values for wake and REM are consistently positive, while N2 and N3 are negative; N1 spans the intermediate range. This polarity is clearer than in the corresponding PC1 distribution (Fig. 1).
- (d) ***Cross-subject consistency.*** A linear mixed-effects model (sleep stage as a fixed effect, participant as a random effect) confirms that stage-dependent differences in IC1 are highly consistent across the cohort, with narrow 95% confidence intervals and uniformly ordered individual slopes.
- (e) ***Three-dimensional IC space.*** Plotting ICs 1–3 shows that wake, REM, and the NREM stages occupy distinct, though partially overlapping, regions. Each component spans a different axis of variation, collectively capturing the multidimensional structure of sleep states (see Fig. S4 for detailed loadings and stage profiles).

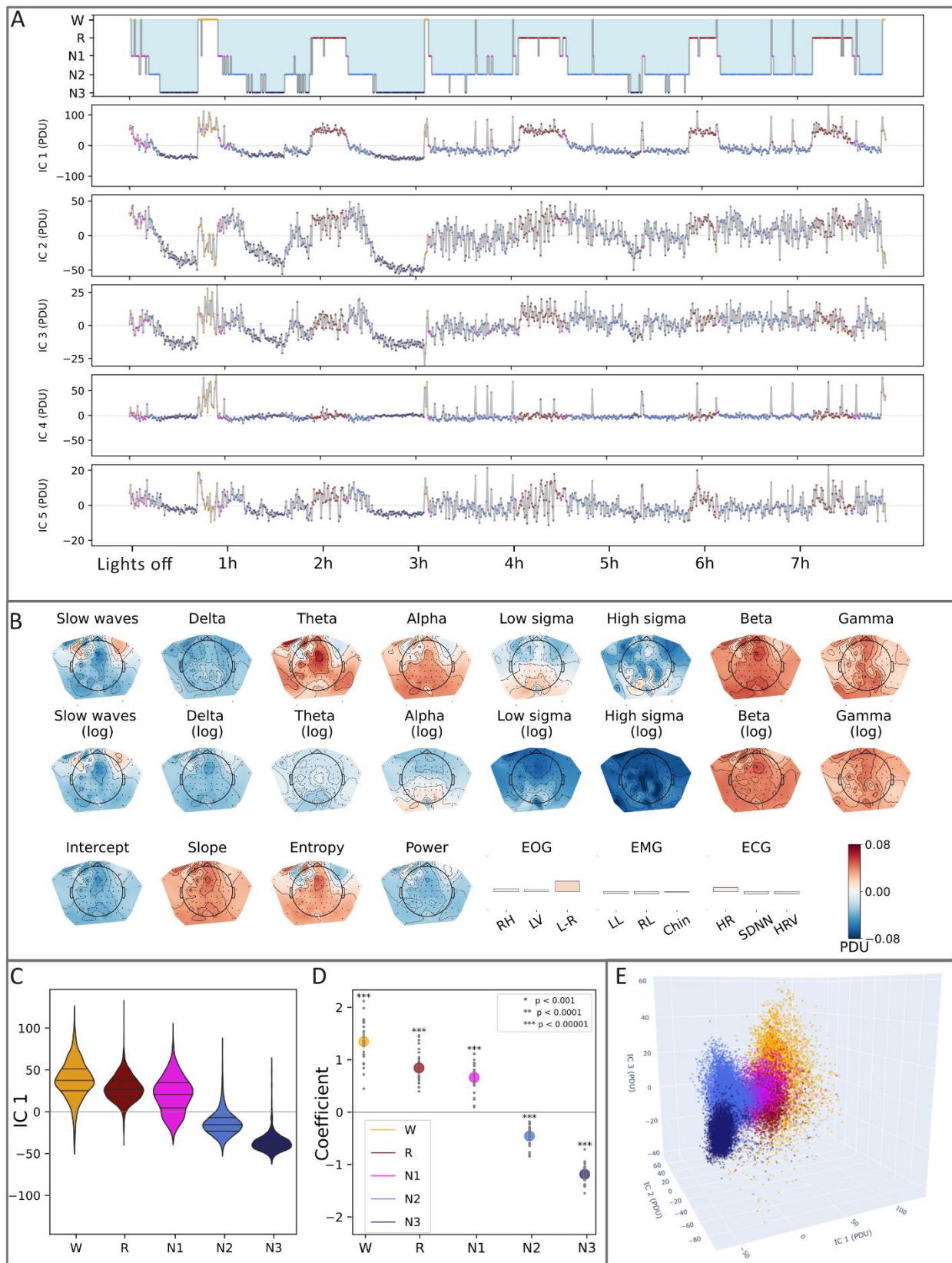


Figure 3 – The hidden states at 30 seconds

The Gaussian hidden Markov model (GHMM) states at the 30s resolution.

(a) **Composition of hidden states.** State 0 is predominantly comprised of wake epochs, state 3 is mainly REM and contains the largest proportion of N1, state 1 is chiefly N2, and state 2 is largely N3.

(b) **State-to-state transitions.** Self-transition probabilities are shown within each node; arrows denote transitions with probability > 0.001 , and arrow width proportional to probability. Most links are markedly asymmetric ($2 \rightarrow 0$, $3 \rightarrow 1$, $0 \rightarrow 1$, $1 \rightarrow 2$), one is roughly balanced ($0 \leftrightarrow 3$), and one is effectively absent ($2 \leftrightarrow 3$).

(c) **Overnight distribution.** Across subjects, state 0 (wake) is more prevalent during lights-off and pre-awakening periods, state 3 (REM/N1) increases steadily through the night, state 2 (N3) declines during the night, and state 1 (N2) shows a gentle rise across the middle of the night. These patterns mirror the conventional stage distribution in Fig. S7A.

(d) **Mean feature maps.** For each state, mean feature values were computed from epochs with posterior probability ≥ 0.99 (or the top 1% if none exceeded that threshold). The sleep stage maps are provided in Fig. S8 for reference to the canonical stages.

State 0 (wake)—The low delta, high gamma, posterior alpha, elevated heart rate (HR) and, EMG power match the wake map.

State 3 (REM/N1)—dominant central theta and beta, matching the REM map.

State 1 (N2)—pronounced high-sigma activity over mid-parietal and lateral frontal sites, matching the N2 map.

State 2 (N3)—strong slow-wave dominance and a steep negative spectral slope contrasting low- and high-frequency power, matching the N3 map.

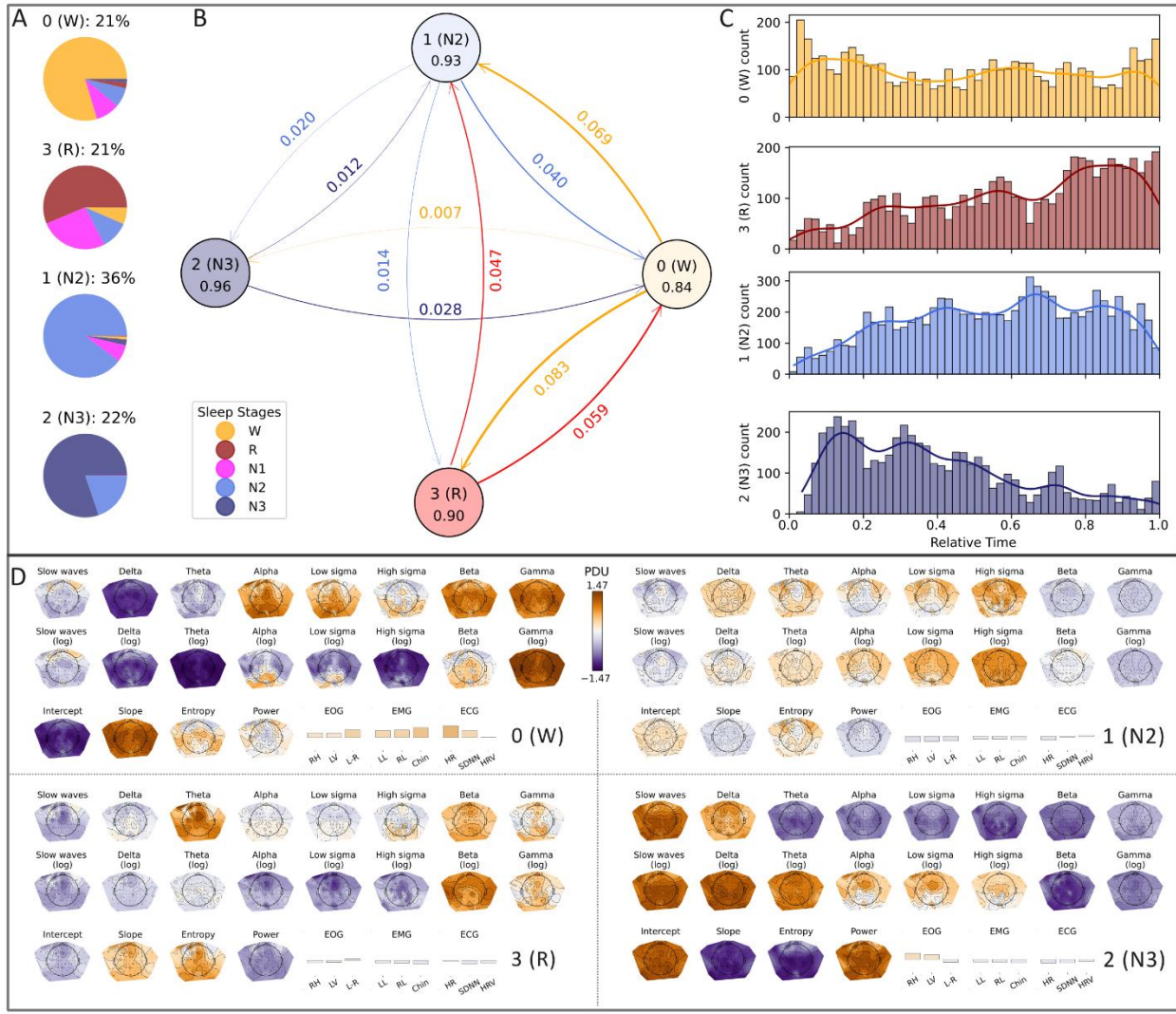


Figure 4 — Micro-state architecture in IC space (4-s epochs).

(a) Overnight prevalence. The stacked-area plot shows the occurrence of the 11 hidden micro-states (S0–S10) obtained from the 4-s Gaussian hidden Markov model (GHMM), normalised from lights-off (0) to final awakening (1).

(b) State composition. For each micro-state, a pie chart gives the percentage of manual stages overlapping with that state. All but four states are stage-dominant; the mixed states are:

- 3 (N2 + N3)
- 7 (REM + N1 + N2)
- 9 and S1 (wake + N1 + REM)

(c) Transition structure.

Top: Qualitative graph. The number inside the node represents the self-transition probability (state stability). Arrow width corresponds to transition probability (> 0.001). The states are ordered by their assigned stage, temporal density (early/late), and stage stability. State colour represents the similarity to the canonical stage map (see Fig. S8 and Figs. 5 and 6).

Bottom. Transition-probability heatmap ($P > 0.001$ only). Most high-probability links connect more similar states, and although probabilities are asymmetric, most edges are bi-directional at this threshold.

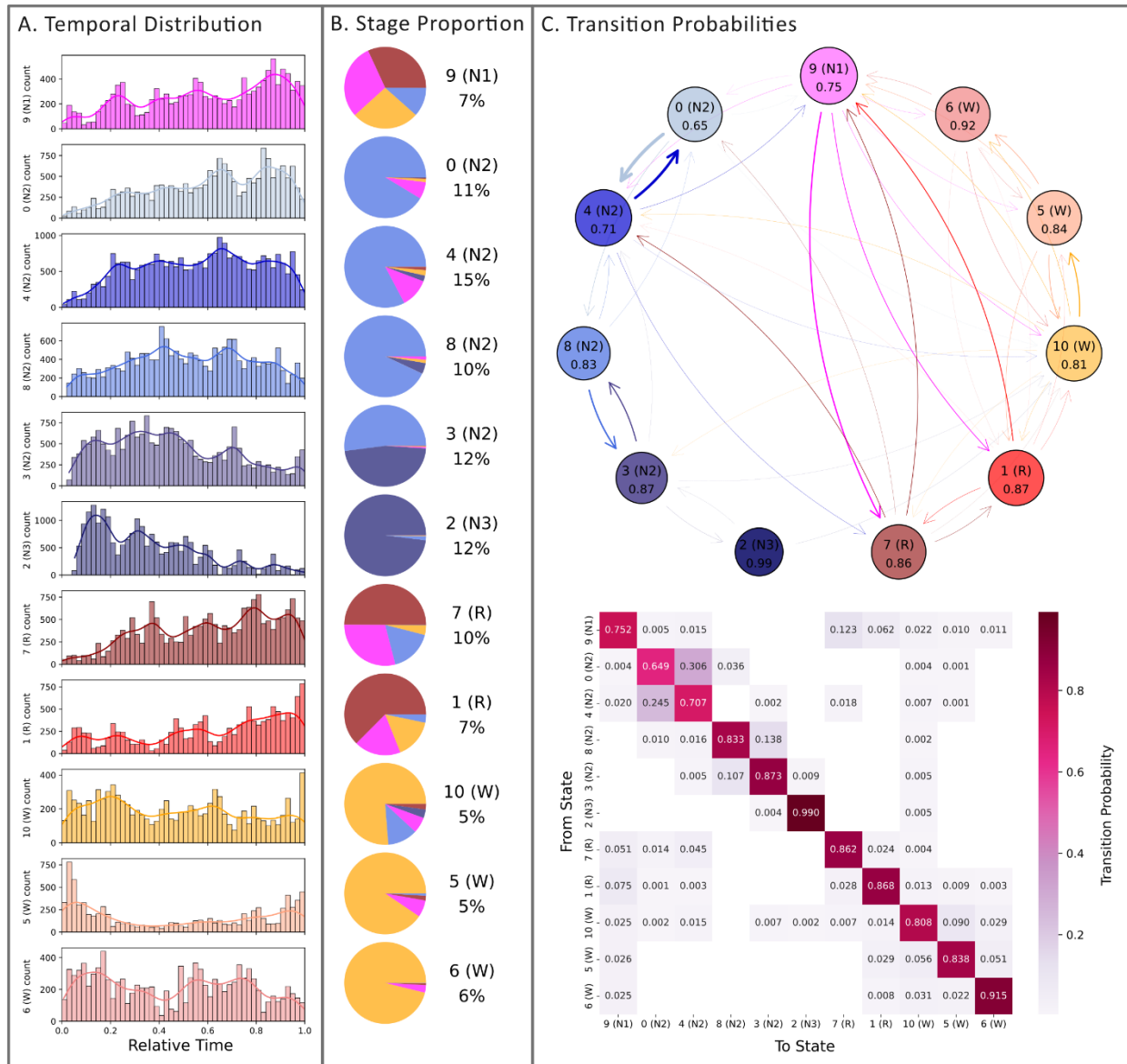


Figure 5— Activated micro-states in IC space (4-s epochs)

For each of the 11 independent component (IC)-space micro-states, we extracted all segments whose posterior probability exceeded 0.99 (or the top 1 % when none reached that threshold) and averaged their overnight z-scored feature vectors. Five activated states—two REM-like and three wake-like—are presented here.

1. REM-like states:

Both REM-like states peak late at night and are mainly entered from state 9 (N1) or each other.

- ***State 7 (tonic-REM)*** – diffuse rise in theta and beta power with a broadband alpha to sigma reduction; EOG remains quiescent, fitting tonic-REM descriptions that lack rapid eye movements. Transition to this stage is also probable from state 4, a slow wave activity (SWA)-rich state.
- ***State 1 (phasic-REM)*** – the posterior gamma and beta surge, a fronto-central theta increases, and positive EOG activity are consistent with phasic-REM physiology.

2. Wake-like states:

State 5 occurs mainly at the beginning and end of the night, while states 6 and 10 occur throughout the night.

- ***State 6 (quiet wake-global alpha)*** – global alpha increases with mild beta rise and minimal peripheral activation (EOG, EMG, ECG).
- ***State 5 (quiet wake-posterior alpha)*** – Focal posterior alpha and diffuse gamma rise, with a mild increase in HR.
- ***State 10 (active wake)*** – large EMG, EOG, and ECG elevations with bilateral central gamma and shallow delta rise; represents an aroused wake configuration. This state is unique as all other states can reach it.

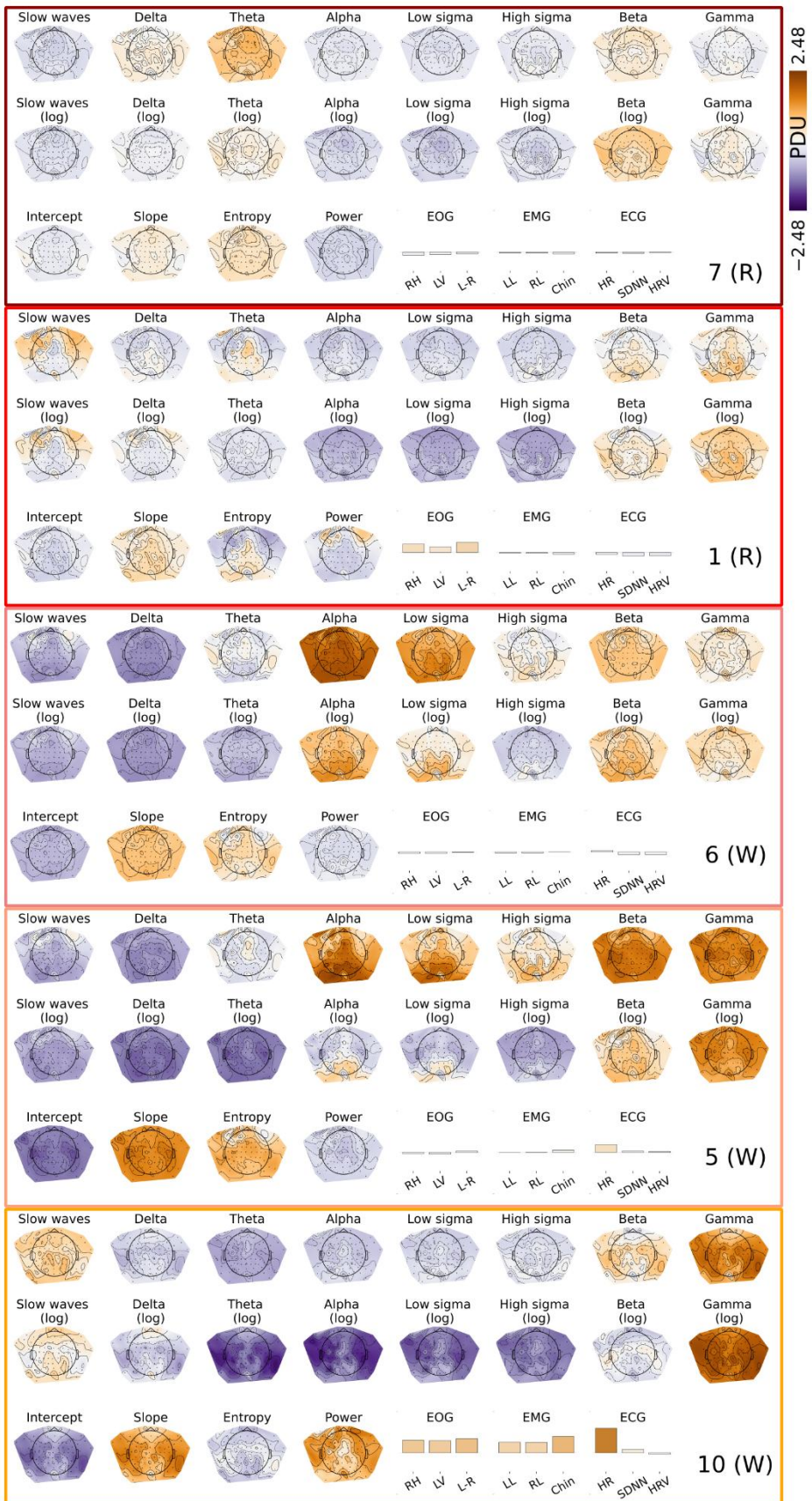


Figure 6— NREM micro-states (IC space).

Using the same criterion as Fig. 5, six NREM-related states cluster into three spectral subtypes:

1. High-frequency NREM – State 9 (N1-like)

- Elevated beta, with reduced delta and slow wave activity (SWA) with a relatively shallow (high) spectral slope
- It occurs during N1, REM, and wake; its occurrence increases throughout the night.

2. Slow-wave NREM – States 2, 3, 4

- Dominated by slow waves and a steep negative slope, entropy is low.
- States 2 (N3) and 3 (N2) peak early (first sleep cycle) and are entered only from N2 and active wake (Fig. 4).
- State 4 prevalence rises as the night advances, and it has relatively low stability (0.707), showing a high transition rate to the spindle dense state 0.

3. Spindel-NREM – States 0, 8

- Focal high sigma power increases over mid-parietal/lateral frontal regions.

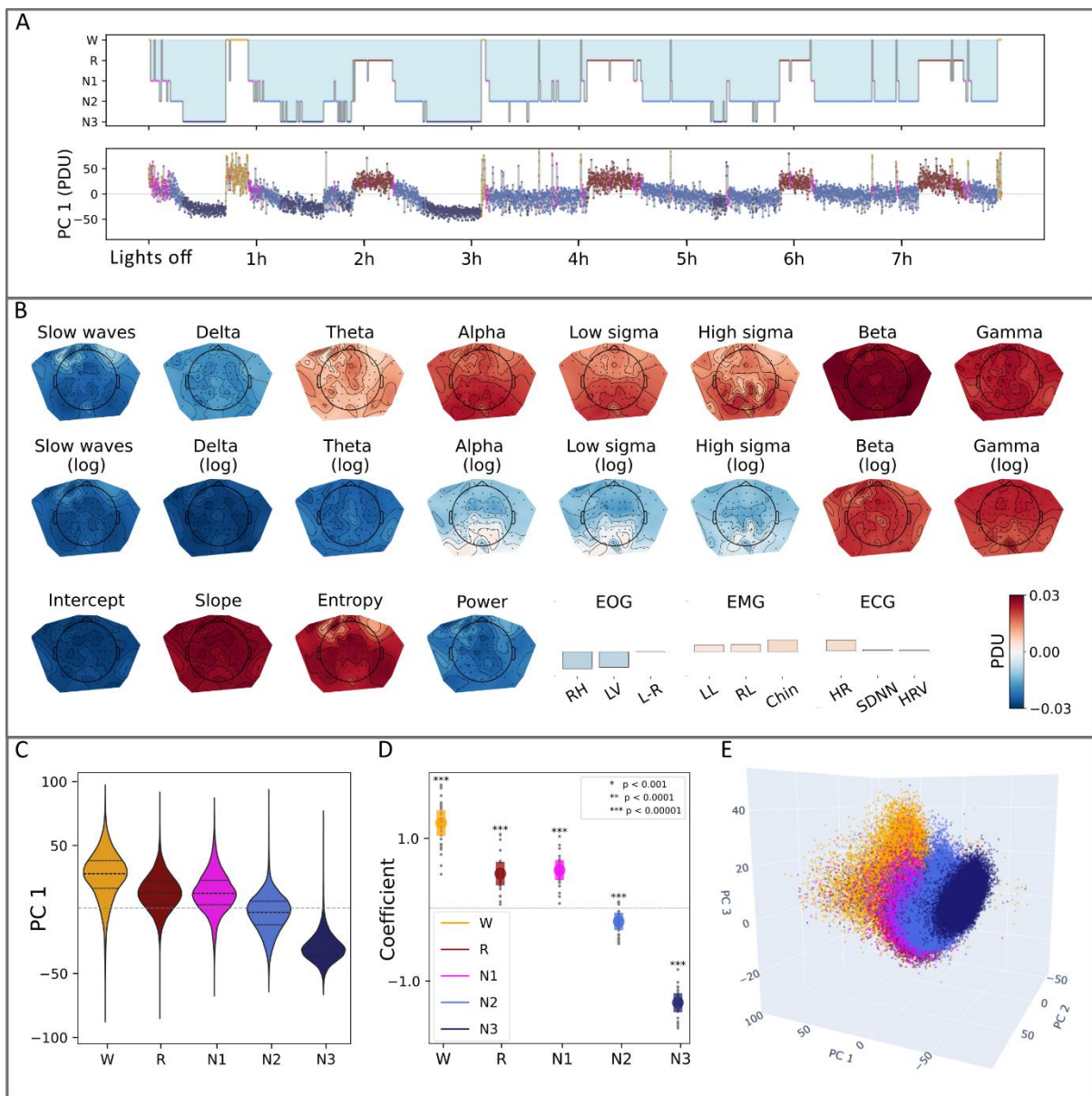
State 0 prevalence rises towards morning, mirroring the reported overnight spindle density and sigma power increases.



Supplementary information

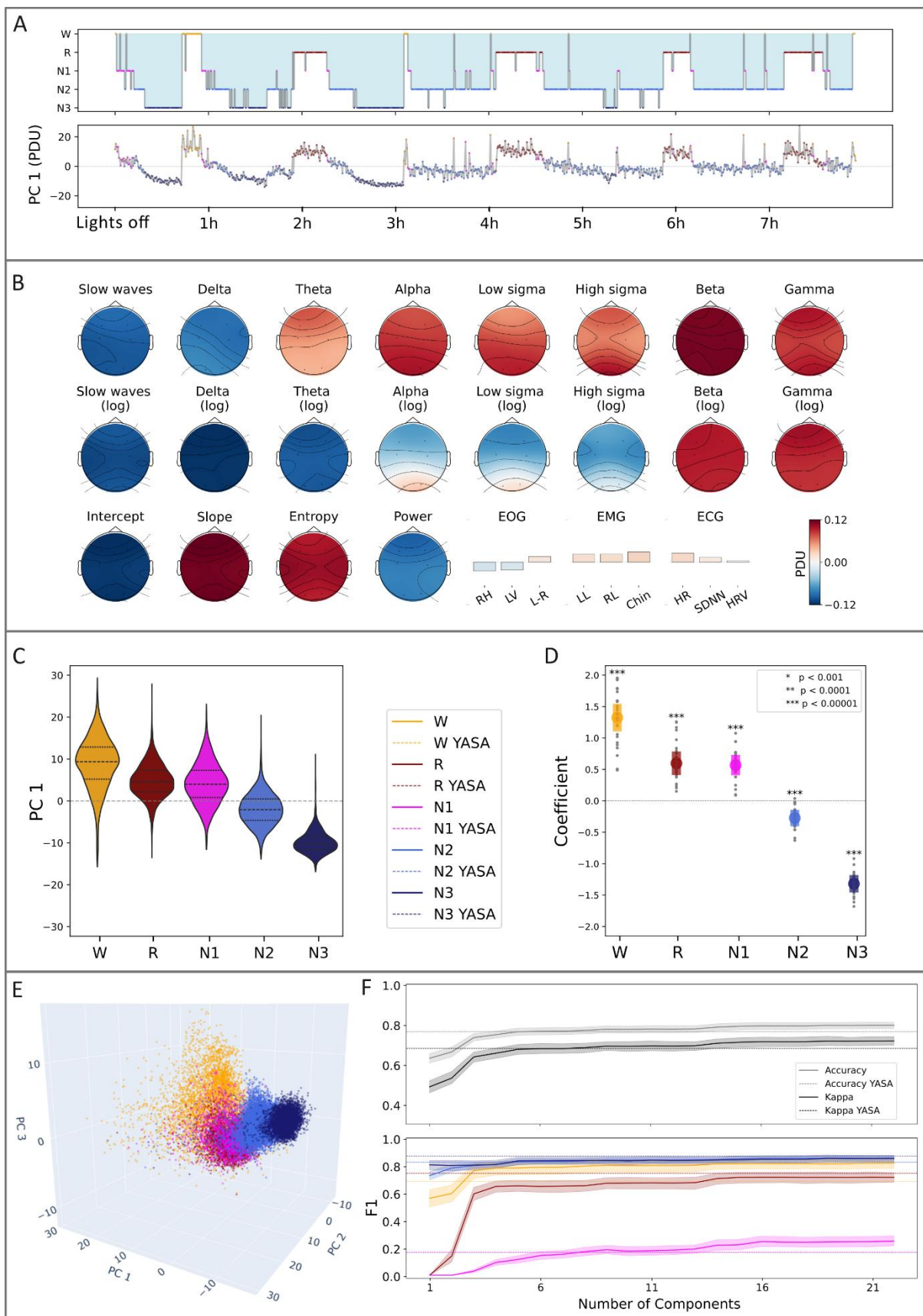
Supplementary Figure S1—Principal-component analysis at 4-s resolution

- (a) **Hypnogram versus Hypno-PC.** Manually scored hypnogram (upper trace) and the first principal component (PC 1, “Hypno-PC”) derived from features computed in 4-s epochs. PC 1 continues to track sleep–wake transitions faithfully, albeit with greater within-stage variability attributable to microstate fluctuations and/or a reduced signal-to-noise ratio at this finer temporal scale.
- (b) **PC1 loading map.** Spatial–spectral loadings resemble those obtained from 30-s epochs (Fig. 1): positive weights over high-frequency bands and the spectral slope. Negative weights over low-frequency activity and total power.
- (c) **Stage-wise distribution of PC1 across participants.** Wakefulness remains clearly separated from N2–N3, whereas N1 and REM sleep overlap substantially, mirroring the 30-s analysis.
- (d) **Cross-subject consistency.** A linear mixed-effects model—with sleep stage as a fixed effect and participant as a random effect—confirmed that PC1 values, at the 4-s resolution, keep the stage mapping and exhibit consistent trends across individuals. Coloured dots indicate the estimated mean slope for each stage, with error bars representing the 95% confidence interval. Grey dots show individual subject-level slopes.
- (e) **Three-dimensional PCA space (PCs 1–3).** The overall arrangement of stages in this space recapitulates that seen with 30-s epochs, but clusters are more diffused, highlighting greater intra-stage variability at 4 s.



Supplementary Figure 2—Principal-component analysis using a standard six-electrode PSG montage

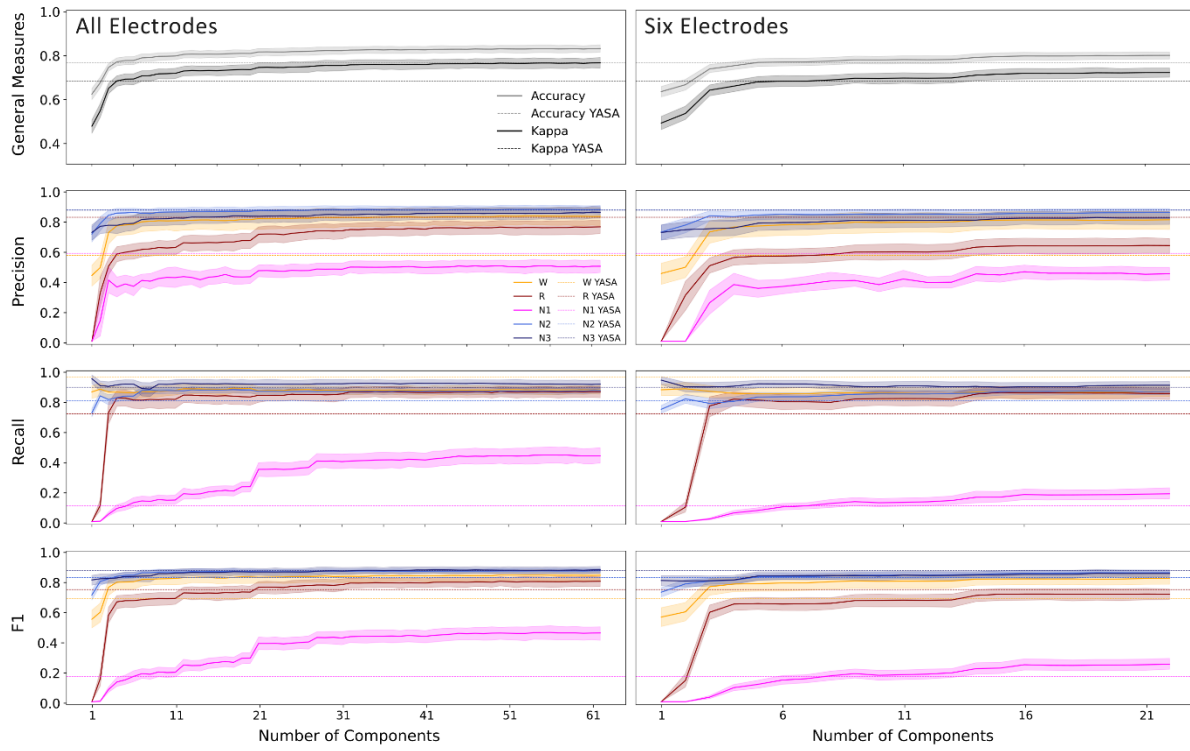
- (a) **Hypnogram versus Hypno-PC.** Manually-scored hypnogram (upper trace) and , principal component (PC) 1 (“Hypno-PC”) derived from spectral features recorded with the six-electrode montage (F3, F4, C3, C4, O1, O2). PC1 retains its characteristic profile: high values during wakefulness and REM sleep and lower values during deep NREM (N3), mirroring the pattern obtained with the full high-density array.
- (b) **PC1 loading map.** Spatial–spectral loadings derived from the reduced montage preserve the dominant contrast between high-frequency (wake/REM) and low-frequency (slow-wave sleep) activity, albeit with diminished spatial resolution.
- (c) **Stage-wise distribution of PC 1 across participants.** Wakefulness remains clearly separated from N2–N3; REM and N1 continue to overlap, replicating the full-montage findings.
- (d) **Cross-subject consistency.** A linear mixed-effects model—with sleep stage as a fixed effect and participant as a random effect—confirmed that PC1 values, based on six electrodes, still span the sleep stages and exhibit consistent trends across individuals. Coloured dots indicate the estimated mean slope for each stage, with error bars representing the 95% confidence interval. Grey dots show individual subject-level slopes.
- (e) **Three-dimensional PC space (PCs 1–3).** Conventional stages form distinct clusters within the reduced PC space, although N1 and REM still encroach upon one another.
- (f) **Stage separability.** The results of a leave-one-out cross validation with a linear support-vector machine (SVM) trained in the six-electrode PC space yield only a modest reduction in accuracy and Cohen’s κ compared to the high-density configuration, however, it remains comparable to the YASA benchmark.



Supplementary Figure 3—Comparison between PCA-based linear SVM classifiers and the YASA algorithm

Left-hand panels (high-density EEG). Linear SVM classifiers were trained on an increasing number of principal components (PCs 1–63) derived from the full high-density montage. Mean performance across participants (solid line) and 95% confidence intervals (shaded band) are shown for overall accuracy and Cohen's κ , together with stage-specific precision, recall (sensitivity), and F1-score for Wake, REM, N1, N2, and N3. Horizontal dashed lines mark the corresponding metrics (mean over subjects) obtained with the YASA algorithm, tested with its recommended channels (C4–M1 EEG, LOC–M2 EOG, submental EMG), plus age and sex metadata.

Right-hand panels (six-electrode montage: F3, F4, C3, C4, O1, O2). The same analysis was repeated using PCs extracted from a clinically routine six-electrode configuration. Although performance is marginally lower than with the high-density array, classification remains robust and continues to approach YASA's benchmark. Notably, YASA exhibits higher sensitivity to wakefulness (0.96) but lower precision (0.57), whereas the PCA– support-vector machine (SVM) approach balances these two metrics more evenly. These results demonstrate that effective automatic staging with a simple classifier can be achieved with markedly fewer electrodes, supporting the method's suitability for large-scale and clinical applications.



Supplementary Table S1—Comparison of YASA and PCA–SVM stage-wise performance (five principal components)

Mean stage performance metrics for the YASA algorithm and for linear support-vector-machine (SVM) classifiers trained on the first five principal components (PCs) at two electrode densities: *all* EEG channels and a routine six-electrode montage (F3, F4, C3, C4, O1, O2). Overall κ and accuracy are shown, followed by stage-specific precision, recall (sensitivity), and F1-score for Wake, REM, N1, N2, and N3. Values are averaged across participants.

Measures by stage						
Model [kappa, accuracy]	Measure	W	R	N1	N2	N3
YASA [0.681, 0.763]	Precision	0.570	0.823	0.583	0.872	0.870
	Recall	0.956	0.715	0.105	0.800	0.891
	F1	0.685	0.744	0.167	0.824	0.870
1 PC all electrodes [0.473, 0.619]	Precision	0.437	0.000	0.000	0.711	0.723
	Recall	0.860	0.000	0.000	0.721	0.947
	F1					
		0.547	0.000	0.000	0.708	0.808
1 IC all electrodes [0.513, 0.649]	Precision	0.437	0.006	0.000	0.789	0.727
	Recall	0.920	0.000	0.000	0.762	0.907
	F1					
		0.568	0.000	0.000	0.768	0.787
1 PC six electrodes [0.487, 0.630]	Precision	0.450	0.000	0.000	0.725	0.722
	Recall	0.874	0.000	0.000	0.744	0.938
	F1	0.562			0.726	0.804
			0.000	0.000		
1 IC six electrodes [0.382, 0.543]	Precision	0.327	0.000	0.000	0.698	0.666
	Recall	0.717	0.000	0.000	0.607	0.942
	F1					
		0.424	0.000	0.000	0.638	0.770
	Precision	0.772	0.591	0.381	0.852	0.780

5 PCs all electrodes [0.687, 0.772]	Recall	0.856	0.819	0.101	0.832	0.912
	F1	0.795	0.670	0.145	0.838	0.831
63 PCs all electrodes [0.762, 0.826]	Precision	0.831	0.758	0.495	0.874	0.856
	Recall	0.874	0.860	0.431	0.869	0.914
	F1					
5 PCs six electrodes [0.675, 0.763]	0.840	0.798	0.452	0.869	0.877	
	Precision	0.765	0.565	0.351	0.839	0.784
	Recall	0.847	0.805	0.074	0.826	0.913
22 PCs six electrodes [0.717, 0.795]	F1	0.783	0.651	0.116	0.828	0.834
	Precision	0.806	0.635	0.448	0.854	0.818
	Recall	0.865	0.849	0.184	0.863	0.903
	F1	0.818	0.714	0.249	0.856	0.851

Supplementary Table S2—Interclass correlation (ICC) of conventional overnight metrics (30-s epochs)

Model	TST	SOL	WAS O	SE	NREM 1	NREM 2	NREM 3	NREM	REM
All SVM (5 stages, n=5)	0.959	0.478	0.778	0.908	0.061	0.826	0.354	0.817	0.355
All SVM (5 stages, n=63)	0.967	0.914	0.924	0.921	0.335	0.882	0.606	0.955	0.765
Six SVM (5 stages, n=5)	0.943	0.275	0.749	0.870	0.060	0.799	0.396	0.808	0.330
Six SVM (5 stages, n=22)	0.963	0.757	0.908	0.915	0.098	0.886	0.535	0.886	0.098
YASA (5 stages)	0.397	0.896	0.321	0.274	0.029	0.532	0.552	0.357	0.614
All ICA- GHMM (4 states, n=5)	0.954	0.949	0.874	0.907	0.0	0.721	0.447	0.624	0.265
Six ICA- GHMM (4 states, n=6)	0.908	0.933	0.779	0.828	0.0	0.787	0.446	0.654	0.281

n – the number of components used for modelling

Across all approaches, the linear SVM that used the full high-density montage and retained every principal component required to explain 90% of the variance (63 PCs) yielded the strongest agreement with manual scoring. It attained near-perfect intraclass correlations for total sleep time (0.967), SOL (0.914), WASO (0.924), and sleep efficiency (0.921), and exceeded 0.88 for each conventional NREM index, with REM reaching 0.765. Reducing the model either to the first five PCs of the same montage or to a conventional six-electrode configuration incurred only modest losses: the six-electrode variant with 22 PCs still achieved ICCs of 0.963 for TST, 0.757 for SOL, and 0.915 for SE, comfortably surpassing YASA on every metric except wake detection, while the five-PC versions remained competitive for global measures, but showed diminished fidelity for the SOL and REM stage.

The minimally supervised four-state ICA–GHMM necessarily merges N1 and REM and, therefore, records no agreement for the NREM-1 category and lower ICCs for REM (0.265–0.281). Nevertheless, its temporal modelling allows it to rival the supervised SVMs for TST (0.954 with all electrodes) and SE (0.907), and to outperform every alternative—including YASA and the 63-PC SVM—in estimating SOL (0.949 with all electrodes, 0.933 with six electrodes). YASA, by contrast, shows high concordance only for SOL (0.896) and REM (0.614), but lags markedly on all other overnight metrics.

Supplementary Table S3—Samples per subject and portion in sleep stage

Subject	30 seconds	4 seconds	%W	%R	%N1	%N2	%N3
EPCTL01	952	7140	0.048	0.185	0.078	0.495	0.194
EPCTL02	1017	7627	0.192	0.069	0.083	0.484	0.173
EPCTL03	761	5707	0.074	0.167	0.087	0.401	0.272
EPCTL04	735	5512	0.310	0.101	0.129	0.291	0.169
EPCTL05	729	5467	0.064	0.181	0.097	0.424	0.233
EPCTL06	886	6645	0.166	0.151	0.087	0.422	0.174
EPCTL07	891	6683	0.127	0.117	0.108	0.446	0.203
EPCTL08	786	5895	0.159	0.101	0.106	0.425	0.210
EPCTL09	910	6825	0.175	0.151	0.107	0.455	0.113
EPCTL10	881	6607	0.285	0.049	0.115	0.308	0.244
EPCTL11	774	5805	0.174	0.096	0.066	0.385	0.279
EPCTL12	748	5610	0.221	0.108	0.099	0.340	0.233
EPCTL13	829	6218	0.204	0.111	0.052	0.440	0.193
EPCTL14	728	5460	0.110	0.130	0.084	0.408	0.268
EPCTL15	730	5475	0.188	0.088	0.095	0.426	0.204
EPCTL16	820	6150	0.043	0.202	0.139	0.473	0.143
EPCTL17	911	6832	0.141	0.076	0.052	0.559	0.173
EPCTL18	586	4395	0.469	0.061	0.070	0.234	0.166
EPCTL19	914	6855	0.244	0.151	0.146	0.312	0.148
EPCTL20	924	6930	0.075	0.152	0.102	0.511	0.161
EPCTL21	831	6232	0.108	0.122	0.088	0.451	0.231
EPCTL22	899	6742	0.098	0.160	0.118	0.468	0.156
EPCTL23	828	6210	0.268	0.097	0.126	0.362	0.147
EPCTL24	936	7020	0.173	0.112	0.131	0.468	0.115
EPCTL25	858	6435	0.348	0.125	0.105	0.296	0.126
EPCTL26	892	6690	0.281	0.114	0.133	0.327	0.143
EPCTL27	895	6713	0.295	0.171	0.115	0.266	0.153
EPCTL28	708	5310	0.093	0.144	0.065	0.544	0.154
EPCTL29	834	6255	0.255	0.120	0.085	0.329	0.211
Mean Subject	715.45	6472.41	0.186	0.125	0.099	0.405	0.186

How these samples were used:

Support-vector-machine (SVM) classifiers and **Gaussian hidden Markov models (GHMMs)** were trained in a leave-one-subject-out (LOOCV) framework. For every LOOCV fold, all epochs from 28 subjects served as the **training** set; the held-out subject formed the **test** set.

It is important to note that the GHMM training was fully unsupervised, and stage labels were never used during model fitting or state-number selection. After training, each hidden state was *named* by gathering the single “most typical” epoch per **training** subject (highest posterior probability), amounting to < 0.6% of labels at 30-s resolution (4 of \approx 715 epochs) and < 0.2 % at 4-s resolution (11 of \approx 6,472 epochs). These minimal labels were used solely to map hidden states onto conventional stage names (Wake, N1, etc.) for interpretability reasons; all performance metrics were evaluated on the **test** subject and, therefore, reflect genuine out-of-sample evaluation.

Supplementary Figure S4—Feature-weight maps and cross-subject consistency for independent components (ICs) 2–5

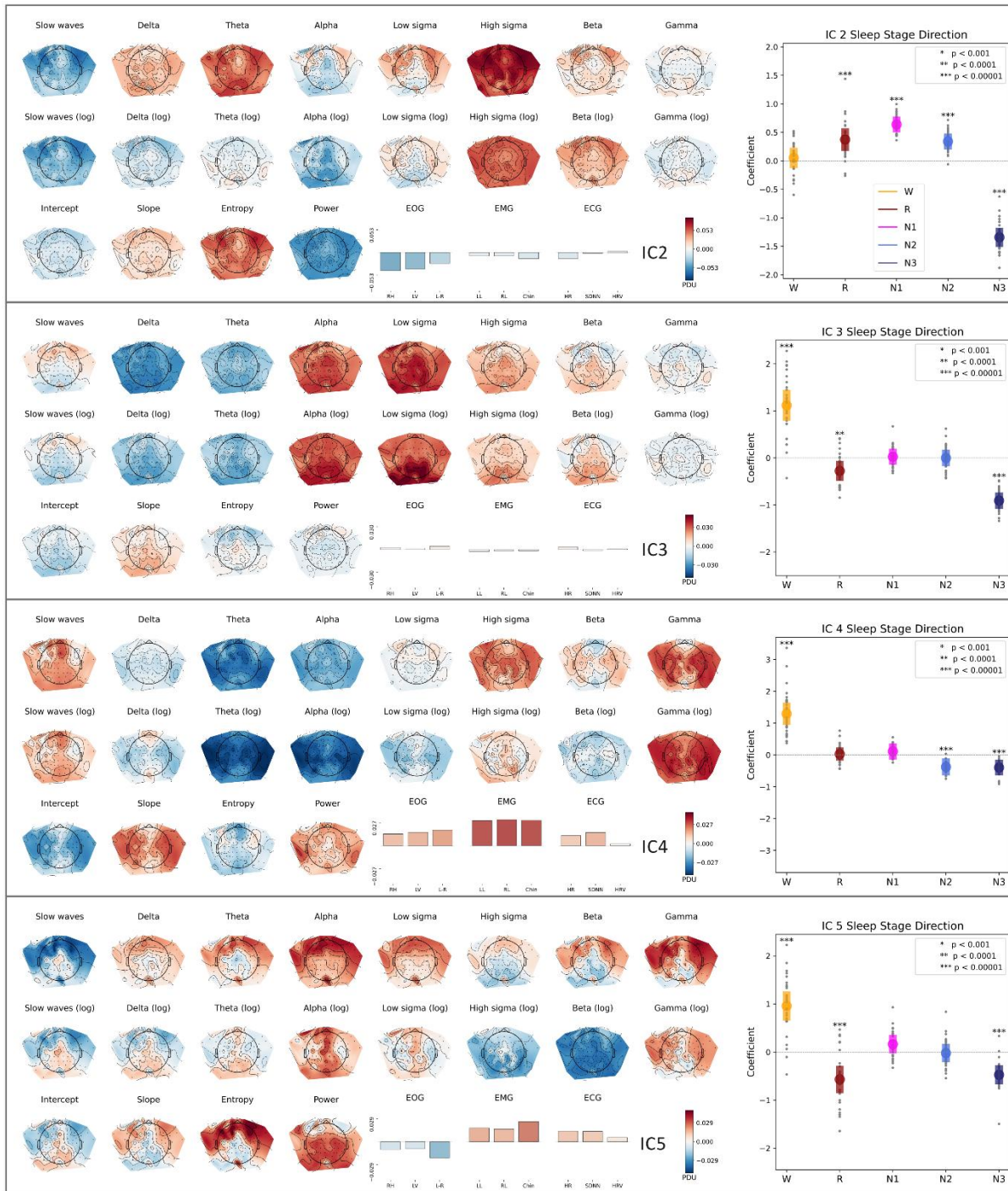
For each component, the left panel shows the topographic loading map (EEG electrode features, EOG, EMG, ECG). The colour scale runs from negative (blue) to positive (red) weights. The right panel displays the linear mixed-effects results: mean stage coefficients (coloured dot) and the 95% confidence intervals (coloured bars) with participant-specific slopes (grey dots), demonstrating the direction and consistency of the stage effects across the cohort.

IC2 Map: Positive weights correspond to N1, N2, and REM and include spectral entropy, theta, and high-sigma power; negative weights highlight frontal slow waves (N3) and posterior alpha (Wake). The mixed-effects plot confirms a graded increase from N3 (negative) to REM (positive) with narrow between-subject scatter and wake showing neutral values.

IC3 Map: Positive weights mark global alpha and low-sigma activity; negative weights emphasise delta–theta power. Non-EEG channels contribute minimally. The mixed-effects results show Wake, REM, and N2 at positive values, with N3 consistently negative.

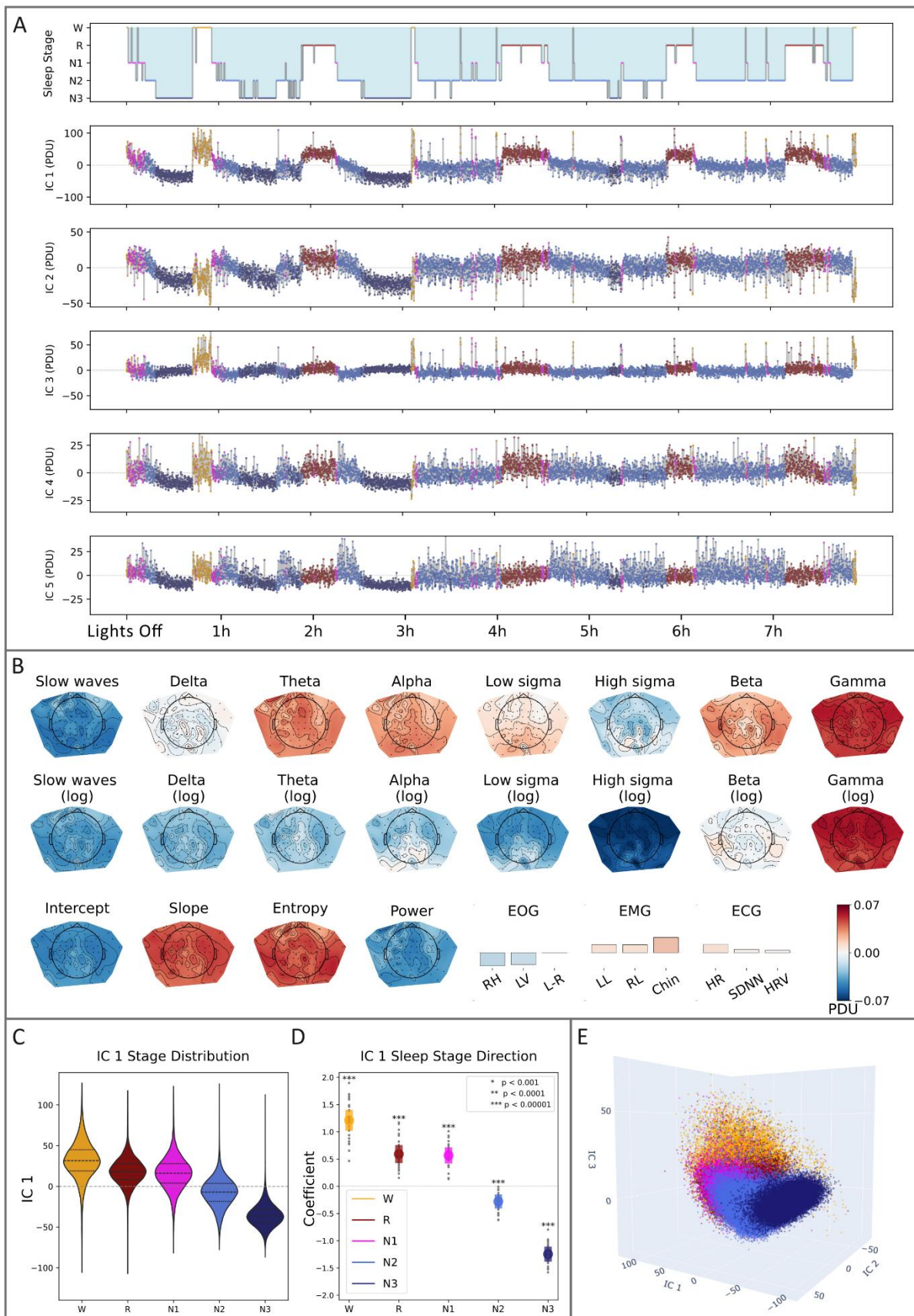
IC4 Map: Positive loadings are dominated by EMG, EOG, heart-rate indices, high-sigma power, and lateral gamma activity, whereas negative loadings are confined primarily to theta activity. In the mixed-effects analysis, wake displays consistently positive values, N1/REM cluster around zero, and N2–N3 lie slightly below zero, reinforcing the view that this component indexes arousal-related activity.

IC5 Map: The mixed-effects model places **Wake** and **REM** at opposite poles with intermediate values for N1–N3. Positive weights index frontal alpha/gamma, posterior broadband power, muscle, and heart activity (Wake); negative weights comprise frontal slow waves, posterior beta/sigma, fronto-central theta, and lateral eye movements (REM).



Supplementary Figure S5—Independent components at 4-s resolution

- (a) **Time-series overview.** The manually scored hypnogram is shown above the five independent components (IC 1–IC 5) obtained by applying ICA to the first five principal components calculated from 4-s epochs.
- IC1** closely follows the hypnogram and, as at 30 s, emphasises the polarity between Wake/REM (positive) and N2–N3 (negative).
- IC2** spans a gradient from N3 (negative) to N1/N2 and REM sleep (positive). It exhibits greater variability in the latter part of the night.
- IC3** shows intermittent positive excursions that coincide with brief arousals.
- IC4** primarily separates Wake from N3 (Fig. S6, IC4) and exhibits its greatest variability during Wake and REM.
- IC5** similarly separates Wake from N3; however, the strongest variability is seen in N2 and Wake, which is strongly related to sigma power activity (Fig. S6, IC5).
- (b) **Feature-weight map for IC1.** Positive loadings are concentrated over posterior alpha, fronto-central theta, and high-frequency power, whereas negative loadings highlight central-posterior sigma and slow waves.
- (c) **Stage distributions of IC1.** Across participants, Wake and REM epochs are consistently mapped to positive IC1 values and N2–N3 to negative values.
- (d) **Cross-subject consistency of IC1.** A linear mixed-effects model (stage fixed; participant random) confirms uniform stage direction across the cohort (coloured dots and bars represent the mean coefficients and the 95% confidence intervals, and grey dots represent the individual subject coefficients).
- (e) **Three-dimensional IC space.** Plotting IC 1, IC 2, and IC 3 reveals distinct, yet partially overlapping, clusters for Wake, REM, and the NREM stages, with each component describing a different axis of sleep-state variability.



Supplementary Figure S6—Topographic loadings and stage consistency for independent components (ICs) 2–5 with 4-s epochs

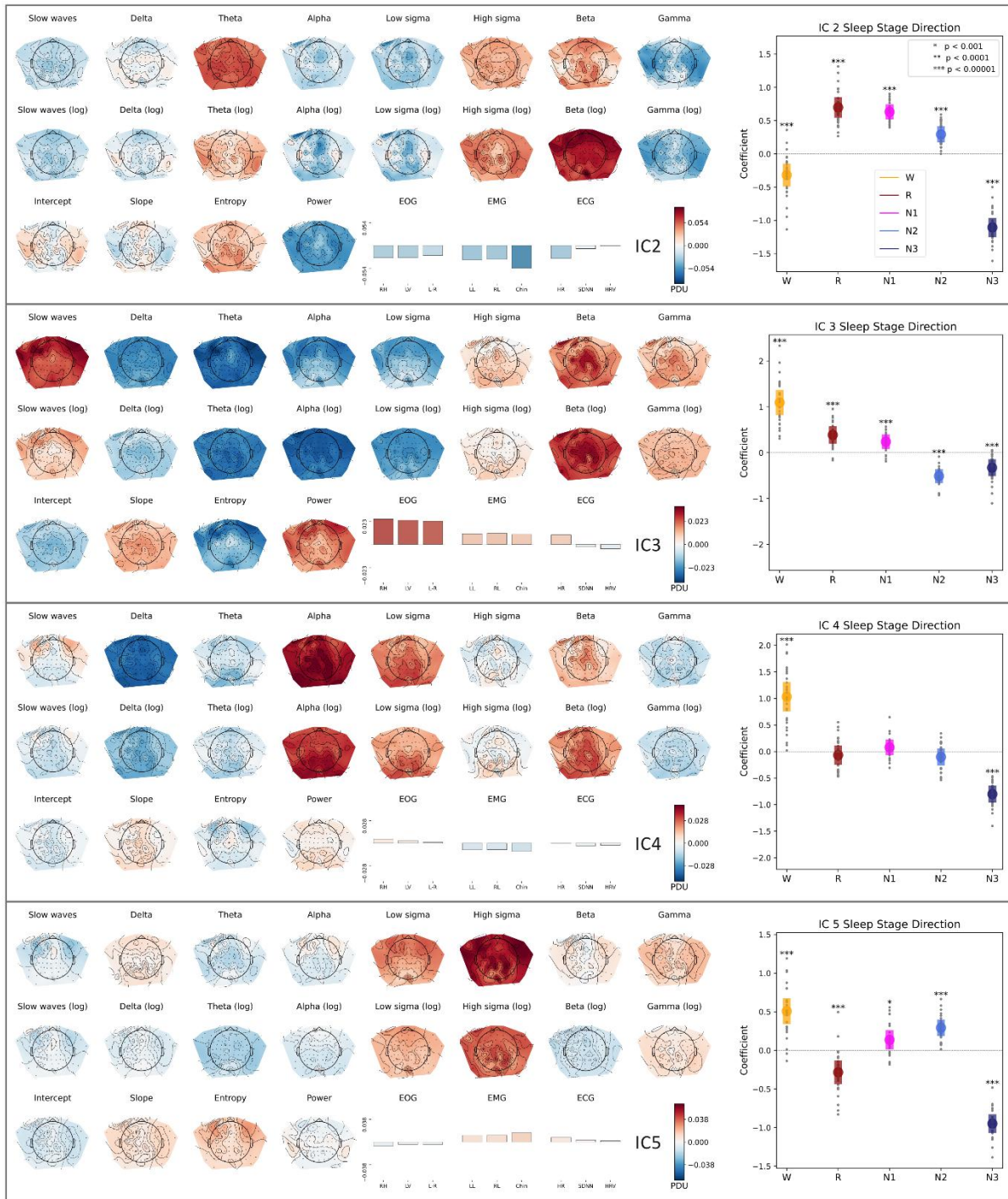
For each component, the left panel shows the topographic loading map (EEG electrode features, EOG, EMG, ECG; blue = negative, red = positive). The right panel gives the linear mixed-effects results: mean stage coefficients \pm 95% CI (coloured bars) with participant slopes (grey dots).

IC2 mixed-effects modelling shows a smooth shift from strongly negative values in N3 to positive values in REM, with Wake clustering towards the negative end of the scale. The positive loadings are dominated by theta and high-sigma power, features typical of N1, N2, and REM. By contrast, the negative loadings combine slow-wave activity (N3) with bilateral gamma, heightened EOG, and particularly, chin EMG activity and an increased heart rate—elements associated with active wakefulness.

IC3 Map: Positive loadings comprise EMG, pronounced EOG, heart-rate indices, slow waves, and beta-gamma power; negative loadings correspond to delta, theta, and alpha activity. Mixed-effects analysis places Wake firmly on the positive side, N1/REM slightly positive, and N2–N3 slightly negative.

IC4 Map: Positive weights concentrate in global alpha and low-sigma and beta bands, whereas negative weights highlight delta power; non-EEG channels contribute only marginally. Wake, REM, and N2 cluster at positive values, while N3 is consistently negative, indicating that this oscillatory process is silenced in deep sleep.

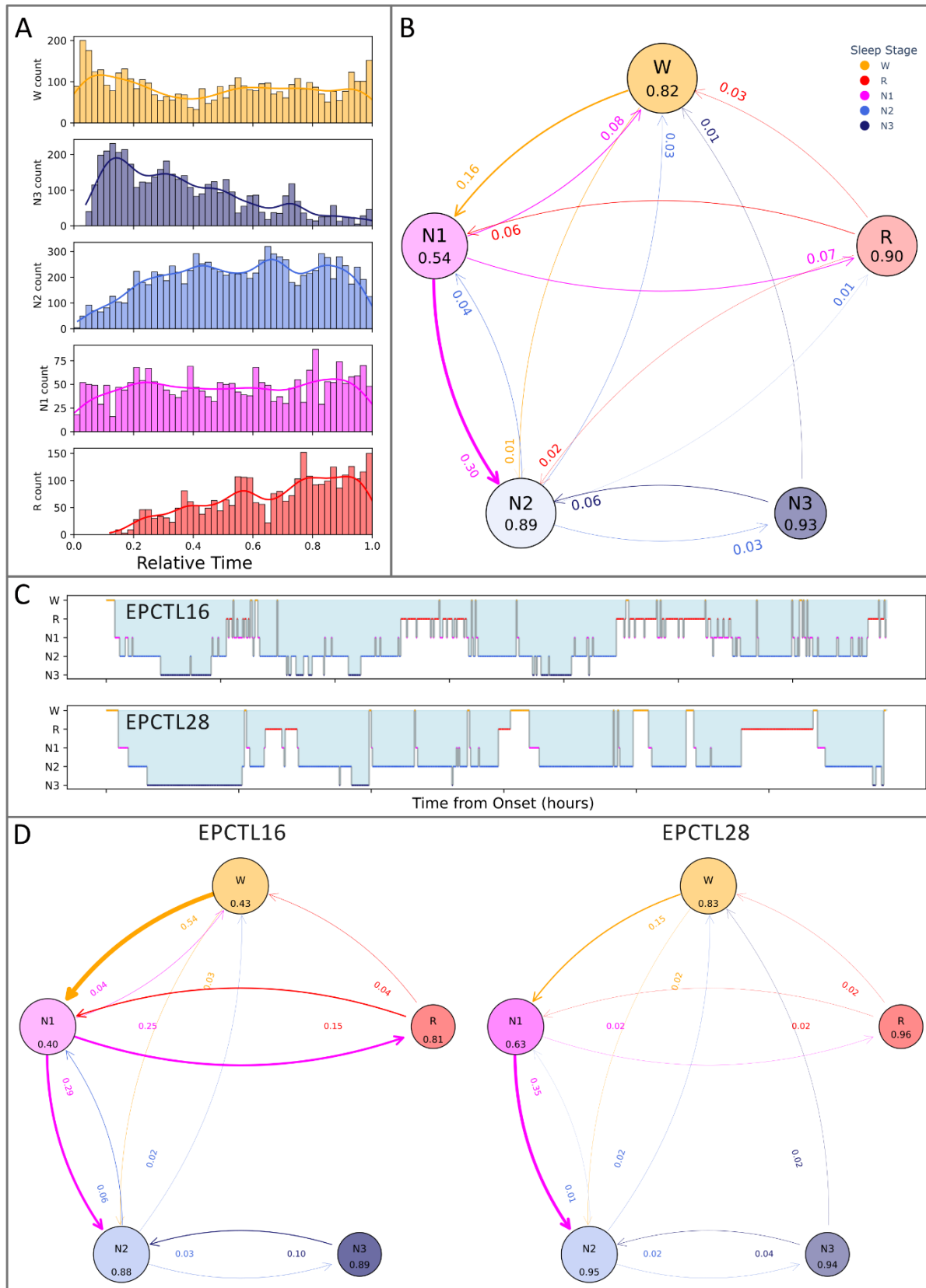
IC5 Map: This component sets Wake and N2 (positive values) against REM and N3 (negative values). Positive values are driven largely by high-sigma power and a modest EMG increase, whereas negatives comprise frontal slow waves, higher spectral entropy, posterior beta/sigma, fronto-central theta, and greater lateral eye movements.



Supplementary Figure 7S—Temporal organisation and transitions of manually scored stages

- (a) Overnight distribution.** Across all participants, the hypnogram shows the expected pattern of pronounced N3 early in the night, followed by a progressive rise in N2 and REM occupancy towards morning.
- (b) Group-average transition graph.** Each node represents a stage; node size is proportional to the number of entries into that stage, and the number within the node gives its self-transition probability (stage stability). Arrow width denotes transition probability (> 0.01 only). N1↔REM are largely balanced, whereas the majority of stage transitions are markedly asymmetric. N3 and REM remain essentially disconnected.
- (c) Individual hypnograms (EPCTL16 vs. EPCTL28).** Both sleepers show high sleep efficiency (96% and 91%), yet EPCTL16 has lower REM continuity, with frequent REM↔N1↔N2 shuttling despite a longer total sleep time and higher efficiency.
- (d) Subject-specific transition graphs.** EPCTL16 displays reduced overall state stability and heightened flux between REM and N1 and N3→N2→N1. Comparing this with EPCTL28 illustrates how transition visualisation reveals nuances not captured by conventional metrics such as TST or WASO, revealing nuances in sleep architecture and stability.

Note: The data presented in this figure are estimated from the sequence of manual sleep labels.



Supplementary Figure S8—Reference feature maps for AASM stages

Topographic spectral-feature maps (EEG, EOG, EMG, ECG) averaged across 29 participants of the canonical sleep stages. These maps provide a reference for interpreting the data-driven state maps in Figs 3D, 5, 6, S10, and S11.

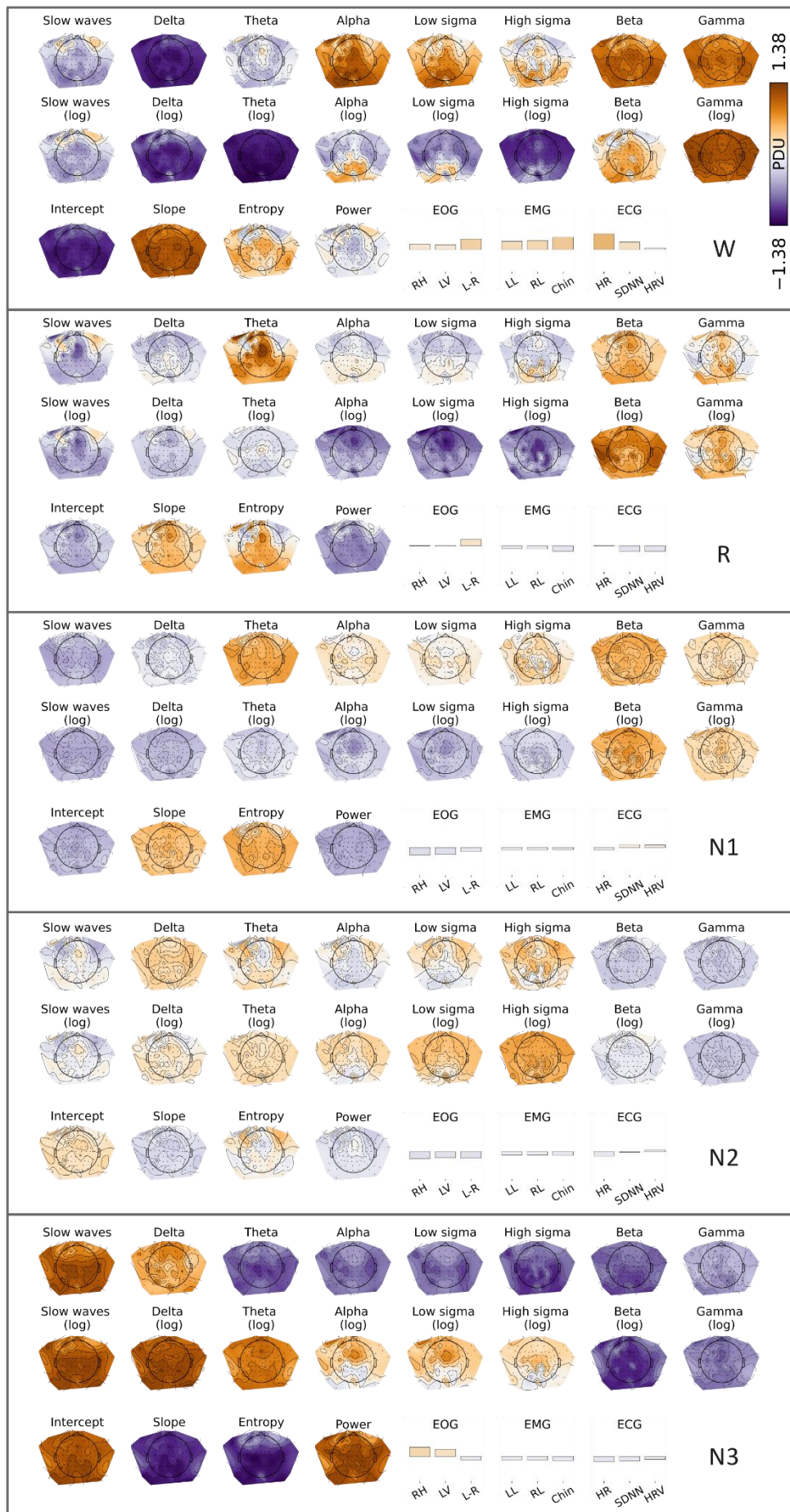
Wake – low delta, high beta/gamma and strong posterior alpha

REM – high fronto-central theta with central-posterior beta/gamma, accompanied by elevated spectral slope and entropy

N1 – global increase in theta and beta power with concomitant rises in entropy and spectral slope. While this map shows increases in similar spectral bands compared to the REM stage, it is missing the spatial specificity that is more evident in REM.

N2 – mainly focal augmentation of sigma (spindle) power over mid-parietal and lateral frontal sites

N3 – dominance of slow-wave activity and a steep negative spectral slope reflecting the balance between low- and high-frequency power.



Supplementary Table S4—Connectivity profile of 4-s microstates in the independent component (IC) space, with a transition probability over 0.001.

For each of the eleven IC-space micro-states the following table lists the number of incoming (in-degree) and outgoing (out-degree) transitions whose probability exceeds 0.001.

- State 10 (active wake) is a hub state, reachable from every other state (in-degree = 10) and able to transition into almost all (out-degree = 9).
- State 9 (N1-like) is the secondary hub (7 in/7 out), further underscoring that Wake-to-N1 and N1-mediated loops are common gateways.
- State 2 (N3) is the most isolated (2 in/2 out), entered only from state 3 (N2-N3) and 10 (active Wake) (Fig. 5C). This pattern supports the view that brief arousals from slow-wave sleep preferentially transition into an activated wake configuration, rather than a quiet-wake sub-state.

State (dominant stage)	Incoming degree	Outgoing degree
10 (W)	10	9
9 (N1)	7	7
4 (N2)	7	6
0 (N2)	6	5
5 (W)	6	4
1 (R)	5	7
7 (R)	4	5
6 (W)	4	4
3 (N2)	4	4
8 (N2)	2	4
2 (N3)	2	2

The number of connections with transition probability > 0.001

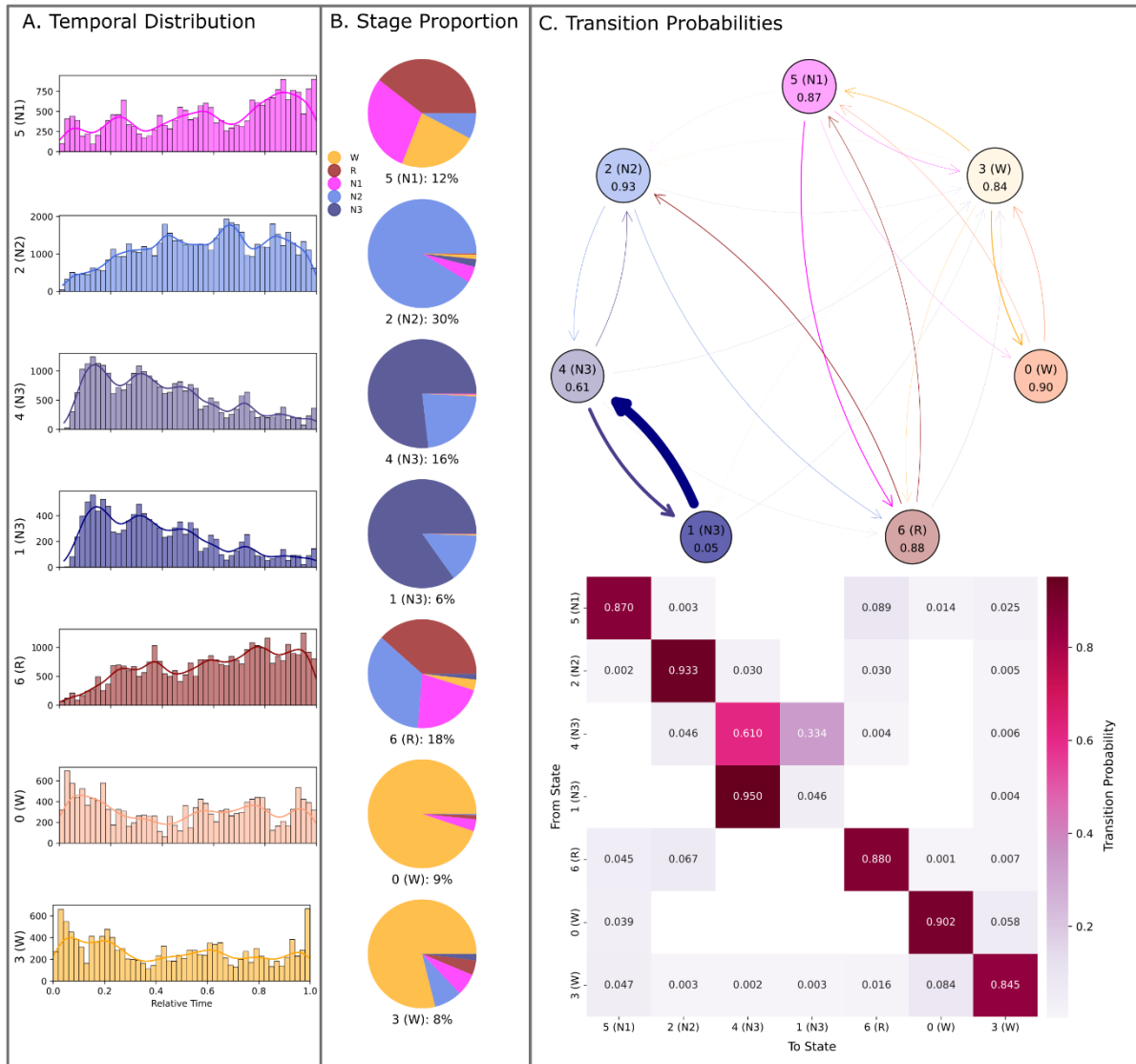
Supplementary Table S5—Edge proportion

Estimating edge proportion and directionality, we can see that for a large number of states, the relative proportion of edges is the state graph lower.

	PCA 30	ICA 30	PCA 4	ICA 4
States	4	4	7	11
Possible edges	6	6	21	55
Total edges	5	5	14	32
Edge proportion	0.833	0.833	0.667	0.582
Bi-directional edge	5	5	12	25
Bi-directional proportion	1	1	0.857	0.781

Supplementary Figure S9— The microstate architecture in the PC space (4-s epochs)

- (a) **Overnight prevalence:** Stacked-area plot of the seven hidden microstates (0–6) extracted from the 4-s principal components (PCs) with a Gaussian hidden Markov model (GHMM), with time normalised from lights-off to final awakening, showing the prevalence of each state throughout the night.
- (b) **State composition:** Pie charts show the proportion of each GHMM-derived state overlapping with manually scored stages. Most states predominantly correspond to a single stage. Exceptions include State 5, which combines Wake, N1, and REM, and State 6, which blends N1, REM, and N2, indicating that these states span transitional or ambiguous regions in sleep architecture.
- (c) **Transition structure:**
- Top:** *qualitative transition graph.* Each node displays self-transition probability; the arrow width represents transition probability between states ($P > 0.001$). Nodes are arranged according to their assigned sleep stage, temporal occurrence (early vs. late), and stability. Node colour reflects similarity to canonical stage feature maps (see Supplementary Fig. S8 and Supplementary Figs. S10–S11).
- Bottom:** transition-probability heat-map. Transitions predominantly occur between physiologically similar states. While the matrix is asymmetric, most observed transitions are bidirectional (0.857, Table 5). Notably, **State 1** shows low stability ($P_{self} = 0.046$), comprising approximately 6% of overnight data—highlighting its role as a transient but recurrent state. **State 3** (active wake) emerges as the central network hub, exhibiting bidirectional transitions with all other states—mirroring the hub-like behaviour observed in the ICA-derived microstates.



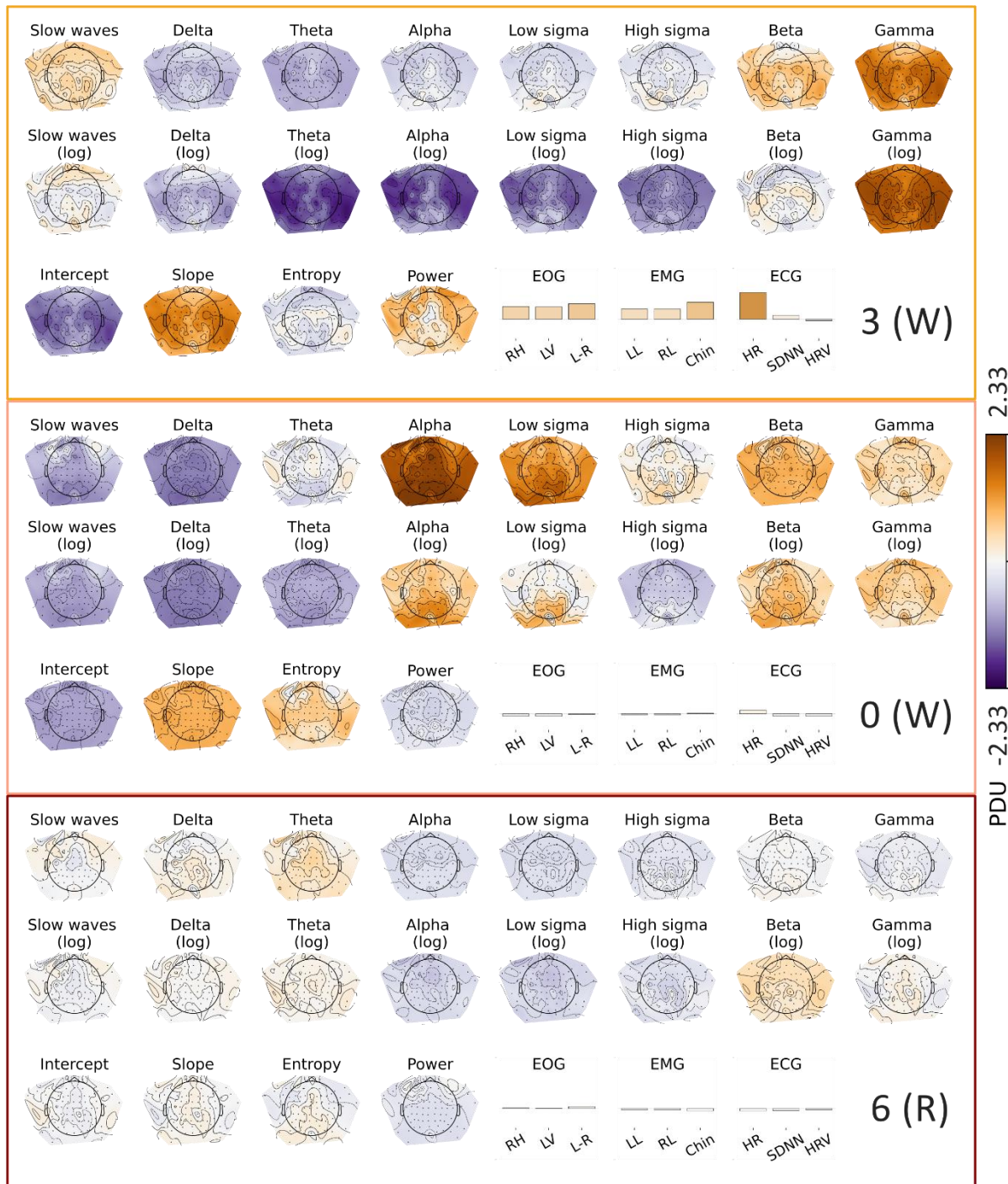
Supplementary Figure S10—Wake and REM microstates in the PC space

Mean feature maps for the principal components (PC) space derived microstates classified as Wake or REM-related. Each map shows the average z-scored feature profile of epochs with a posterior probability > 0.99 or within the top 1 % most likely assignments for that state, as described in Fig. 5.

Active Wake (3) – Marked by elevated EMG, EOG, and heart rate, alongside a widespread increase in beta and gamma power, mainly in bilateral fronto-central distribution.

Quiet wake (0) – Characterised by a focal increase in posterior alpha power with no clear autonomic activation.

REM-like (6) – This state exhibits weak spectral activation, with modest central theta elevation and no distinct eye-movement signature.



Supplementary Figure S11—NREM microstates (PC space)

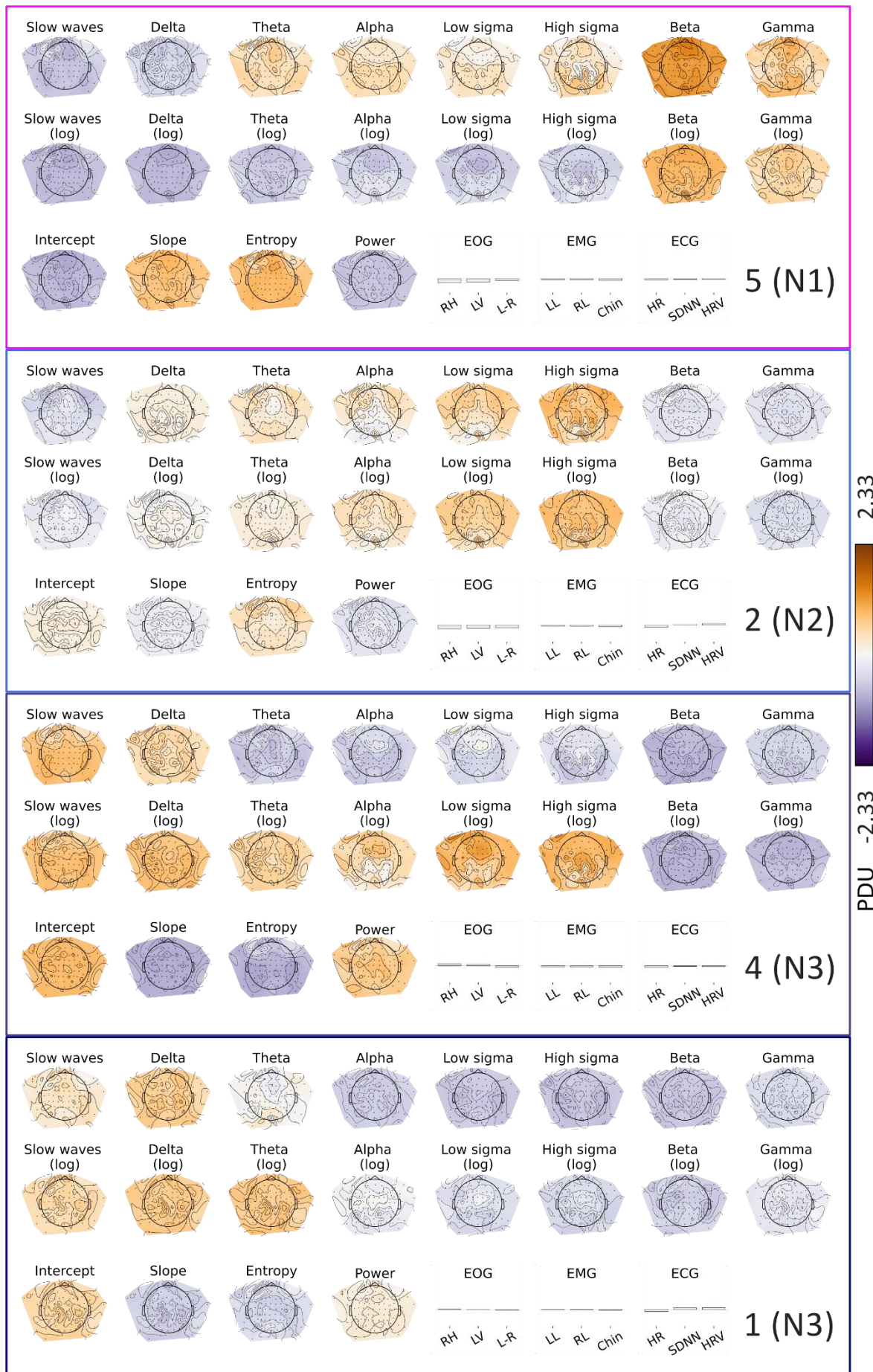
Mean feature maps for principal component (PC) space-derived NREM microstates. Each map reflects the average z-scored feature profile of epochs with a posterior probability > 0.99 or within the top 1 % most likely assignments for that state, as described in Fig. 5.

N1-like (5) – Characterised by beta enhancement and delta suppression. This state closely corresponds to state 9 in the ICA-derived microstates and aligns well with the canonical N1 stage map.

N2-like (2) – Exhibits a classic spindle pattern with elevated sigma power. Unlike the IC-derived states, this representation does not resolve distinct high- and low-sigma subtypes.

N3-stable (4) – Dominated by strong slow-wave activity and a steep negative spectral slope. Although labelled “stable,” this state shows relatively modest self-transition probability ($P_{self} = 0.61$) and frequently transitions into state 1.

N3-unstable (1) – Shows a shallower slow-wave slope, lower alpha and sigma power, and milder slow-wave power compared to state 4. This state shows frequent transitions and is followed by N3-stable (state 4) 95% of the time.



Supplementary Figure S12—The PCA microstates

This figure demonstrates the similarity of the hidden state definition at the 30-second time scale as a comparison to the ICA-derived states. Overall, the state definition is almost identical, with some small differences appearing when comparing sleep measurements. In this plot, there are two differences compared to the ICA states. First, the state numbers are different, which has no practical implications. Second, the estimated transition probabilities are slightly different, and here, the transition from the REM-like state to the N2-like state crosses 0.046 in contrast to the ICA model, which is 0.047 (Fig. 3).

